

1 **Constraining the fluid history of a CO₂-H₂S reservoir: Insights from stable isotopes,**
2 **REE and fluid inclusion microthermometry**

3
4 Carmen Zwahlen¹, Cathy Hollis¹, Michael Lawson², Stephen P. Becker², Adrian Boyce³, Zheng Zhou⁴ and Greg
5 Holland¹

6
7 ¹ The University of Manchester, Oxford Road, M13 9PL Manchester, United Kingdom

8 ² ExxonMobil Upstream Research Company, Spring, Texas, 77389, USA

9 ³ Scottish Universities Environmental research centre (SUERC), Rankine Avenue, G75 0QF East Kilbride, United
10 Kingdom

11 ⁴ Lancaster University, Lancaster Environment Centre, Lancaster University, LA1 4YQ Lancaster, United Kingdom

12 Corresponding author: Carmen Zwahlen (zwahleca@gmail.com)

13 **Key Points:**

- 14 • sulphate sulphur and oxygen isotopes co-fractionated during thermochemical sulphate
15 reduction process
- 16 • The approximate length of TSR is 80 ka
- 17 • A combination of petrography, REE, fluid inclusion and stable isotope measurements can
18 be useful to disentangle the fluid history of a large CO₂ reservoir
19

20 **Abstract**

21 Reservoirs that host CO₂-H₂S bearing gases provide a key insight into crustal redox reactions such as
22 thermochemical sulphate reduction (TSR). Despite this, there remains a poor understanding of the extent, duration
23 and the factors limiting this process on a reservoir scale. Here we show how a combination of petrography, fluid
24 inclusion, rare earth element (REE) and carbon ($\delta^{13}\text{C}$), oxygen ($\delta^{18}\text{O}$) and sulphur ($\delta^{34}\text{S}$) stable isotope data can
25 disentangle the fluid history of the world's largest CO₂ accumulation, the LaBarge Field in Wyoming, USA. The
26 carbonate hosted LaBarge Field was charged with oil around 80 Ma ago, which together with nodular anhydrite,
27 represent the reactants for TSR. The nodules exhibit two distinct trends of evolution in $\delta^{13}\text{C}$ with both $\delta^{34}\text{S}$ and $\delta^{18}\text{O}$
28 that may be coupled to two different processes. The first trend, was interpreted to reflect the coupled dissolution of
29 anhydrite and reduction to elemental sulphur and the oxidation of organic compounds and associated precipitation of
30 calcite during TSR. In contrast, the second trend was interpreted to be the result of the hydrothermal CO₂ influx after
31 the cessation of TSR. In addition, mass balance calculations were performed to estimate an approximate TSR
32 reaction duration of 80 ka and to identify the availability of organic compounds as the limiting factor of the TSR
33 process. Such an approach provides a tool for the prediction of TSR occurrence elsewhere and advancing our
34 understanding of crustal fluid interactions.

35 **1 Introduction**

36 Study of fluid-fluid and fluid-rock interactions in gas reservoirs containing elevated concentrations of CO₂-H₂S not
37 only assists in understanding processes that control migration and accumulation of crustal fluids, but also the
38 feasibility of CO₂-H₂S co-sequestration (Glezakou et al., 2012; Kaszuba et al., 2011; Knauss et al., 2005; Pearce et
39 al., 2016; Williams & Paulo, 2002; Xiao et al., 2009; Zhang et al., 2011). In addition, the formation of H₂S in natural
40 gas reservoirs is of interest for drilling security and the estimation of gas degradation and presence of mineral
41 deposits (e.g. Mississippi Valley-type deposits) (Piqué et al., 2009; Powell & MacQueen, 1984). However, sulphur
42 cycling and redox reactions such as thermochemical sulphate reduction (TSR) are not well understood on a reservoir
43 scale and only a few natural systems have been studied including the Khuff Formation, Saudi Arabia (Bildstein et
44 al., 2001; Jenden et al., 2015; Worden et al., 1995, 2000; Worden & Smalgeoley, 1996), the Smackover Formation,
45 USA (Claypool & Mancini, 1989; Heydari & Moore, 1989), Lower Saxony Basin, Germany (Biehl et al., 2016),
46 Tarim and Sichuan Basin, China (Cai et al., 2001, 2003, 2004, 2009, 2010, 2013, 2016; Hao et al., 2015; Jiang et al.,
47 2014, 2015, Liu et al., 2013, 2014) and the Nisku Formation, Canada (Machel, 1987b, 1987a, 2001; Riciputi et al.,
48 1994). Since the reactions are difficult to simulate experimentally under reservoir conditions, due to their slow rates
49 of reaction (Amrani et al., 2008; Anderson & Thom, 2008; Ding et al., 2008, 2009, Yue et al., 2005, 2006), natural
50 CO₂-H₂S reservoirs form ideal natural analogues for CO₂-H₂S co-sequestration (Allis et al., 2001; Bickle et al.,
51 2013; Kaszuba et al., 2011).

52
53 The LaBarge Field located in western Wyoming, USA hosts an estimated $4.7 \times 10^{12} \text{ m}^3$ (167 trillion cubic feet
54 (TCF)) of gas (Stilwell, 1989), of which 66% is CO₂, in the Mississippian-aged Madison Formation (Fig. 1). While
55 the mineralogy, petrography and sequence stratigraphy of the Madison Formation in Wyoming has been studied
56 comprehensively in the past (Budai & Cummings, 1987; Budai, 1985; Budai et al., 1984; Buoniconti, 2008; Katz,
57 2008; Katz et al., 2007; Smith et al., 2004; Sonnenfeld, 1996b), there is a relative paucity of petrographic
58 observations from the LaBarge Field. The gas forms a 250 m thick gas column and is the largest known natural CO₂
59 accumulation in the world (Allis et al., 2001; Lynds et al., 2010; Stilwell, 1989). Different sources for the CO₂ and
60 H₂S at the LaBarge Field have been proposed including thermal degradation of hydrocarbons, breakdown of
61 carbonates, volcanic gas migration and TSR (De Bruin, 2001; Huang et al., 2007; Stilwell, 1989). Thermochemical
62 sulphate reduction (TSR) is a redox reaction where sulphate is reduced to form hydrogen sulphide and hydrocarbons
63 are simultaneously oxidized to form carbon dioxide (Orr, 1974). The volume of CO₂ in the LaBarge Field exceeds
64 the volume of H₂S by a factor >12, which makes TSR as a single source for CO₂ unlikely given that TSR produces
65 CO₂ and H₂S in a molar ratio less than 1:1 (Liu et al., 2013). Despite these numerous studies, it has so far been
66 difficult to unambiguously determine the origin of these non- hydrocarbon gases in the field.

67 This paper provides new insights into the timing, extent and duration of TSR at the LaBarge Field, which are crucial
68 to improve the general understanding of TSR. The mineralogy and petrography of three drill cores from the Madison
69 Formation will be presented as a precursor to a detailed geochemical characterization of different mineral phases in
70 this formation. The geochemical assessment integrates rare earth element (REE), stable isotope and fluid inclusion
71 analysis to provide new constraints on the sulphate source and the onset of TSR. It will be discussed how this

72 information can be used to estimate the duration of TSR at the LaBarge Field and elucidate the limiting factors
73 during this process. The insights developed by this study may be used to better understand TSR, fluid-fluid and
74 fluid-rock interactions in other systems that have experienced multiple contributions of exogenously sourced fluid.

75 **2 Tectonic and geological setting and burial history**

76 The LaBarge field is located at the north end of the Moxa Arch structure in Wyoming (USA), which is part of the
77 Greater Green River Basin (Fig. 1). On the west side, the LaBarge Field is confined by an eastward plunging
78 basement involved reverse fault (Dixon, 1982; Kraig et al., 1987; Stilwell, 1989) (Fig. 1b). The gas trapped in the
79 LaBarge Field consists on average of 66% CO₂, 21% CH₄, 7% N₂, 5% H₂S and 0.6% He (Huang et al., 2007). The
80 Madison Formation consists of alternating limestone and dolomite (Huang et al., 2007) and exhibits an average
81 porosity of 8-10%, a permeability of 10 - 50 mD and a residual water saturation of 10% (Huang et al., 2007). The
82 limestone and dolomite beds reach a maximum thicknesses of 20 m with dolomite slightly dominating in abundance
83 over limestone. Except for micro-inclusions there is no primary anhydrite left, however, intercalated nodular calcite
84 has been interpreted to represent a replacement of a former anhydrite phase (King et al., 2014; Thayer, 1983). These
85 nodules occur in layers or as single nodules throughout the formation with a slight increase towards the bottom of
86 the formation, but make up only around 0.2% of the total rock volume. Additional former evaporite beds are
87 reported to have been dissolved, as evidenced by the presence of solution collapse breccias, but the volume of these
88 features is more difficult to quantify (Budai & Cummings, 1987; Katz et al., 2006; Middleton, 1961; A. E. Roberts,
89 1966; Smith et al., 2004; Thayer, 1983).

90
91 The Moxa Arch is an anticline with a north-south oriented hinge line that borders the Wyoming fold and thrust belt
92 to the west and the Rock Springs Uplift to the east. The anticline formed during the thick-skinned Laramide
93 deformation from the Campanian until the Eocene (Becker & Lynds, 2012; Campbell-Stone et al., 2011; Kraig et al.,
94 1987). At the same time, the thin skinned Sevier fold and thrust belt migrated east towards the Moxa Arch
95 (Blackstone, 1979; Dixon, 1982; Kraig et al., 1987; Nozaki et al., 1997; Wach, 1977). The most eastern thrust sheet,
96 the Hogsback thrust, overruns the Moxa Arch at the LaBarge Field and displaces the sedimentary section that
97 predates the Triassic (Becker & Lynds, 2012; Kraig et al., 1987). In the late Cretaceous (84 - 76 Ma) Laramide
98 related burial drove the Permian Phosphoria Formation to depths sufficient for oil and gas generation. These fluids
99 migrated down into the Madison Formation due to overpressure during maturation (Johnson, 2005) (Fig. 2). The
100 Pennsylvanian Weber Sandstone Formation overlying the Madison Formation acted as a carrier bed during oil
101 migration but its permeability decreased over time due to cement precipitation until it formed a good seal for fluids
102 hosted in the Madison Formation (Johnson, 2005). A burial history for the Moxa arch region has been established at
103 the Bruff field, 30 km south of LaBarge (Roberts et al., 2005). The burial history is characterized by variable
104 sedimentation rates and erosional events at 92 Ma, 75 Ma, 66 Ma and 5 Ma until today (Roberts et al., 2005). The
105 burial history of the LaBarge Field differs from the Bruff field by an additional 500 m of structural relief in Pliocene
106 times. Maximum burial was reached at 5 Ma with a maximum burial temperature of approximately 215°C (Roberts
107 et al., 2005), whereas the present day temperature of the Madison Formation is approximately 135°C.

108 **3 Samples and Method**

109 **3.1 Samples**

110
111 Host rock limestone, dolomite, pyrite and calcite veins and nodules were sampled from three cores of the Madison
112 Formation from the LaBarge field, located on the crest of the Moxa Arch or slightly off crest (Fig. 1 & 3). In total,
113 20 samples were collected from drill core FC13-10, 12 samples from drill core FC15-28, and 7 samples from drill
114 core LR8-11 (Fig. 1 & 3, Table 1). Drill core LR4-22 was not viewed but one sample of this drill core was available
115 for analysis. The calcite veins and nodules were selected to represent different depths and nodule abundances of the
116 drill cores. Pyrite was mainly found in drill cores FC15-28 and FC13-10 whereas LR8-11 only contained one
117 location suitable for pyrite sampling. Additionally, two native sulphur samples were collected from drill core FC15-
118 28 and FC13-10. All samples were fist size pieces of drill core which were then cut for thin sections. Minerals were
119 identified visually by a Nikon Eclipse LV100NPOL microscope and analytically by a JEOL 6400 scanning electron
120 microscope (SEM) at the University of Manchester. The samples were then cut into smaller pieces of interest and
121 crushed for further analytical measurements. The abundance of anhydrite for TSR has been estimated from calcite
122 that replaced former anhydrite nodules through drill core logging and the amount of pyrite has also been estimated
123 from drill core logging.

124

125 3.2 Stable isotopes

126

127 Carbon ($\delta^{13}\text{C}$) and oxygen ($\delta^{18}\text{O}$) isotope measurements were performed on 32 calcite and dolomite samples on an
128 Isoprime multiflow mass spectrometer at Lancaster University (Table 1). Dolomite samples were first added to 1 M
129 HCl for one hour and rinsed with deionised water to remove any traces of calcite (De Groot, 2008). Following this,
130 400 μg of sample powder were added to phosphoric acid to evolve CO_2 , which was subsequently analyzed. All data
131 was corrected to PDB (Pee Dee Belemnite) using international standards LSVEC ($\delta^{13}\text{C}$ -46.6‰, $\delta^{18}\text{O}$ -26.7‰), NBS
132 18 ($\delta^{13}\text{C}$ -5.014‰, $\delta^{18}\text{O}$ -23.2‰) and CO1 ($\delta^{13}\text{C}$ +2.492‰, $\delta^{18}\text{O}$ -2.4‰). Precision for five standard replicates ($n=5$,
133 1 standard deviation (SD)) was $<0.1\text{‰}$ for carbon and oxygen isotopes.

134

135 Additionally, 17 calcite nodules were analyzed for sulphur ($\delta^{34}\text{S}$) and oxygen ($\delta^{18}\text{O}$) isotopes in carbonate associated
136 sulphate (CAS) (Table 1). A total of 900 mg of crushed sample were dissolved and re-precipitated as BaSO_4
137 following the filtration method of Wynn et al. (2008). Two samples (C7 & A3) did not yield the minimum of 250 μg
138 and 350 μg of BaSO_4 for the sulphur and oxygen isotope analyses respectively. One sample (C9) gave enough
139 BaSO_4 for sulphur isotope analysis but not for oxygen isotope analysis. The isotopic ratios were determined by
140 continuous flow isotope ratio mass spectrometry using the Isoprime 100 mass spectrometer linked to an Elementar
141 Pyrocube analyser at the University of Lancaster (Wynn et al., 2014). Sulphur and oxygen isotopic data are
142 presented relative to V-CDT (Vienna-Canyon Diablo Troilite) and V-SMOW (Vienna-Standard Mean Ocean Water)
143 respectively. The international standards NBS-127 (+21.1‰) and SO_5 (+0.5‰) were used to calibrate sulphur
144 isotope data. For the oxygen isotopes the international standards NBS-127 (+9.3‰) and SO_6 (-11.35‰) were used.
145 The precision for standard replicates ($n=4$, 1SD) was $<0.1\text{‰}$ for sulphur and $<0.2\text{‰}$ for oxygen. Three samples (C4,
146 C5 and C11) contained pyrite grains which oxidized during the preparation procedure and lead to contamination
147 (Marenco et al., 2008) and were therefore excluded.

148

149 Oxygen isotopes were analyzed on three quartz samples on a Finnigan MAT 253 mass spectrometer at the British
150 Geological Survey following the fluorination method described by Clayton and Mayeda (1963) (Table 1). The
151 samples were added to 1 M HCl and rinsed with deionised water prior to analysis in order to remove any calcite
152 from the samples. The data are corrected to V-SMOW using the standard BFC (M. Leng et al., 2001; M. J. Leng &
153 Sloane, 2008) (assumed value 29‰). The precision for standard replicates was $<0.1\text{‰}$ and the sample
154 reproducibility (1SD) was 0.1‰.

155

156 Pyrite sulphur isotope measurements were carried out at Scottish Universities Environmental Research Centre
157 (SUERC) (Table 1). The pyrite samples were converted to SO_2 by combustion under vacuum at 1070 °C with
158 cuprous oxide after the method of Robinson and Kusakabe (1975). The gas was then purified cryogenically and
159 analyzed on a VG SIRA II gas mass spectrometer. The two native sulphur samples were measured in the same way
160 as the pyrites. The sulphur isotopic data were corrected to V-CDT using the international standards NBS-123
161 (+17.1‰), IAEA-S-3 (-31‰) and the internal lab standard CP-1 (-4.6‰).

162

163 3.3 Rare earth elements

164

165 Rare earth element concentrations in 15 calcite nodules were measured on an Agilent 7500cx ICP-MS at the
166 University of Manchester (Table 1 & 2, Fig. 4). 100 mg of crushed calcite sample was digested overnight in 5 ml of
167 6 M HCl. A subsample of the liquid phase was extracted and diluted to a $<0.1\%$ TDS solution for analysis. Typical
168 relative errors for REE standard concentrations were less than 5%. The concentrations were normalized to Post-
169 Archean Average Australian Shale (PAAS) (McLennan, 1989; Nance & Taylor, 1976). Two samples (C1 & A3)
170 exhibit very low REE concentrations (on the same level as the measured blanks) and are therefore excluded from the
171 following interpretation. In three samples (A2, C14 & C10) the Ho concentration is below the blank level and was
172 also excluded from this interpretation. In 8 samples the europium concentration was corrupted by barium oxide
173 interference (Dulski, 1994; Jarvis et al., 1989)(Fig. 4b). In these samples the Ba concentration is up to 2200 ppm and
174 shows an almost perfect linear correlation with the Eu concentration ($R^2=0.98$) (Fig. 4e). The remaining 5 samples
175 (C4, C5, C6, C11 & C12) lie above this trend with a low Ba concentration and are considered reliable.

176

177 4.3 Fluid inclusions micro thermometry

178

179 Fluid inclusion homogenisation temperatures were measured on double polished thin sections at ExxonMobil
180 Upstream Research Company (Texas, USA) and Fluid, Inc. (Colorado, USA) (Table 3). The fluid inclusion analyses
181 were conducted on different samples than the REE and stable isotope measurements except for sample Q2. Fluid
182 inclusion analysis was performed following the fluid inclusion assembly (FIA) method described by (Goldstein &
183 Reynolds, 1994) and reported as the range of homogenisation temperatures found in the assemblage with the number
184 of inclusions observed (Table 3). This technique consists of finding the highest homogenization temperature (T_h) for
185 aqueous, methane-bearing, fluid-inclusion assemblages. The temperature at which the fluid inclusion was trapped is
186 recorded in the homogenization temperatures of aqueous fluid inclusions. Fluid inclusions examined in this study
187 occur as both primary and secondary inclusions in different mineral phases (dolomite, quartz, fracture-filling calcite,
188 fluorite and calcite that replaced anhydrite). Because gas inclusions are present in all observed phases coexisting
189 with many of these aqueous inclusion assemblages, the assumption is that no pressure correction is required, and
190 thus the T_h value represents a true original trapping temperature along the water liquid-vapor saturation (or bubble
191 point) curve. Thus, primary inclusions represent an original crystallization temperature of the mineral growth zone
192 in which they are hosted, and secondary inclusions potentially represent a maximum temperature post-
193 crystallization. The homogenization temperatures of aqueous fluid inclusions can provide accurate estimates of
194 maximum temperature at peak burial or record the process of some anomalous temperatures not related to burial,
195 such as hydrothermal activity.

196 **4 Results**

197 *4.1 Mineralogy and petrography*

198 The Madison Formation in the LaBarge Field is dominated by skeletal packstone (Fig. 3a & b). The bioclasts are 50
199 - 300 μm in size and include foraminifers and brachiopods, bivalve and echinoderm fragments. All skeletal grains
200 are micritized except for some echinoderm fragments (Fig. 3a & b). All primary inter- and intraparticle porosity is
201 cemented by micro-spar. Based on the viewed drill cores, approximately 60% of the Madison Formation limestone
202 is pervasively dolomitized (Fig. 3c). The dolomite is finely crystalline and equigranular with a crystal size of
203 approximately 50 μm . The crystal shapes are euhedral whereas some micritized skeletal grains are replaced by
204 subhedral dolomite (Fig. 3c). The dolomite is fabric preserving and can have high intercrystalline porosity. Part of
205 this porosity is subsequently filled with poikilotopic calcite cement with crystal sizes up to 3 mm (Fig. 3d). Bedding
206 parallel low (0.5 cm) and high (3 cm) amplitude stylolites are found mainly in the limestone but occur also in the
207 dolomite.

208 In addition to limestone and dolomite, silicified limestone occurs in three different forms: bedding parallel bands of
209 silicified limestone, chalcedony and quartz along the rim of former anhydrite nodules and silicified dolomite breccia.
210 The silicified limestone bands are bound by stylolites and consist of mainly 20 μm to 100 μm anhedral quartz
211 crystals. These crystals are precipitated around and partially replacing skeletal grains. They are mainly found in drill
212 core FC15-28 and LR8-11 around 140 m and 250 m beneath the top of the Madison Formation. The second silica
213 form consists of chalcedony rosettes 1 mm in diameter and submillimeter, anhedral and sometimes radially oriented
214 quartz crystals. The chalcedony and quartz crystals are precipitated in the rims of former anhydrite nodules and in
215 one case replaced the former anhydrite nodule completely (Fig. 3h). This silica form encompasses significant
216 volumes of anhydrite and some fluorite inclusions and is most abundant in drill core FC13-10. The third silica form
217 is a silicified dolomite breccia composed of in-equigranular concretion of <200 μm sized anhedral quartz crystals
218 surrounded by equigranular 10 μm sized anhedral quartz crystals (Fig. 3e). The coarser quartz crystals sometimes
219 form pseudomorphs of quartz after dolomite. The dolomite around the quartz forms concretions of coarser dolomite
220 surrounded by very fine grained dolomite. This suggests that the quartz is not brecciated itself but replaced and
221 cemented a dolomite breccia. The dolomite breccia replacing quartz occurs in all three drill cores at 2123 m, 1913 m
222 and 2001 m true vertical depth subsea (TVD SS) in drill cores FC15-28, LR8-11 and FC13-10, respectively. These
223 depths correspond to approximately 176 m depth from the top of the Madison Formation in all three drill cores.
224 Beside the micro-spar there are two more forms of authigenic calcite: fracture-filling calcite and calcite that replaced
225 anhydrite. The fracture-filling calcite forms subhedral blocky calcite crystals up to several centimetres in diameter
226 that are precipitated in fractures in the limestone and dolomite host rock (Fig. 3f). Sparse pyrite, galena and apatite
227 micro-inclusions and quartz and fluorite crystals are enclosed by this calcite phase. This phase is abundant in drill
228 cores FC15-28 and FC13-10 but has not been found in drill core LR8-11.

229 Fluorite is found in two different forms at two different times in the paragenetic sequence: the first occurrence is as
230 inclusions in quartz, fracture-filling calcite and calcite that replaced anhydrite and the second occurrence is as
231 fracture-filling fluorite. The inclusions are up to 15 μm in size and sometimes associated with anhydrite inclusions.

232 The fluorite cemented fracture consists of 1 mm sized anhedral crystals and crosscuts and fills a reopened calcite-
 233 cemented fracture in drill core FC15-28 at 2120.1 m TVD SS. Subhedral saddle dolomite crystals, 5 mm in size, are
 234 found in drill core FC13-10 at 2057 m TVD SS. The saddle dolomite encloses quartz, fluorite and fracture-filling
 235 calcite crystals.

236 The former anhydrite nodules are completely replaced by calcite except for some micro-inclusions (Fig. 3g & h &
 237 Appendix). This calcite phase exhibits anhedral to subhedral crystals from 100 to 500 μm in size with an
 238 interlocking fabric. Two calcite nodules have a centimetre sized calcite crystal in the centre (Fig. 3h). This calcite
 239 phase has abundant pyrite, anhydrite and fluorite inclusions of up to 25 μm , 50 μm and 15 μm in size, respectively.
 240 Additionally there are a few <20 μm sized dolomite, celestine, sylvite, sylvenite, barite and apatite inclusions. In the
 241 chalcedony and quartz-rimmed nodules, the calcite encloses some of the silica crystals.

242 Pyrite and minor amounts of sphalerite are found at the base of the Madison Formation in all three drill cores, and
 243 are most abundant in drill core FC15-28. The pyrite and sphalerite form up to 1 mm sized subhedral to euhedral
 244 crystals. Pyrite is precipitated along and within reopened stylolites and is often associated with solid bitumen. In
 245 calcite that replaced anhydrite, pyrite is also located within calcite crystals and on crystal boundaries. The pyrite is
 246 present as dissemination in the host rock and sometimes overgrows fine dolomite grains. Sphalerite is found
 247 precipitated along with pyrite in the same mineral associations, but is not present in all sites of pyrite mineralisation.
 248 Solid bitumen is found as small concretions alongside stylolites, crosscutting fracture-filling calcite and in pores of
 249 the calcite that replaced anhydrite. Native sulphur was found in two places: in between calcite that replaced
 250 anhydrite crystals in drill core FC15-28 at 2153.2 m TVD SS (Fig. 3g) and within a pyrite and solid bitumen vein in
 251 drill core FC13-10 at 1830.4 m TVD SS (Table 1).

252 4.2 Rare earth elements and Yttrium

253 All rare earth elements and yttrium (REEY) concentrations are normalized to PAAS (Table 2). The fracture-filling
 254 calcite (samples C6 and C12) and the calcite that replaced anhydrite (C4, C5, C11, A1(C), A1(F), A2, C2, C8, C9,
 255 C10 and C14) show distinct REE patterns (Fig. 4). The two fracture-filling coarse crystalline calcites (samples C6
 256 and C12) have a flat REEY pattern with distinct negative cerium and positive yttrium anomalies (Fig. 4a). The
 257 patterns are similar to seawater measurements except for a relative depletion in heavy rare earth elements (HREE)
 258 (Mitra et al., 1994; Schmidt et al., 2007) (Fig. 4a). The Y/Ho ratios for the two samples are 52 and 72, which is in
 259 the range of seawater (44-74) (Bau and Dulski, 1995). These samples plot in the far right corner of the Ce-Pr-
 260 anomaly diagram (Bau and Dulski, 1996) which is in the range of seawater values (Fig. 4e). The total concentration
 261 in REE in these samples is 65 and 19 ppm.

262 The REEY patterns of the majority of the calcite that replaced anhydrite samples (A1(C), A1(F), A2, C2, C8, C9,
 263 C10 and C14) are characterized by a flat to slightly convex upward shaped pattern with a slight increase from light
 264 rare earth elements (LREE) to HREE (Fig. 4b). The Y/Ho ratios lie in the range of seawater values (Bau and Dulski,
 265 1995), with the exception of two samples (C2 and C9) that have a Y/Ho ratio of 31 and 89. Three samples (C8, C9
 266 and C14) from drill core LR8-11 plot in the negative cerium anomaly field in the Ce-Pr-anomaly diagram (Bau and
 267 Dulski, 1996), whereas the rest of the samples exhibit no cerium anomaly (Fig. 4e). The mean absolute REE
 268 concentration in these samples is 2 ppm (0.6 to 5.9, n=12). In sample A1 the rim (A1(F)) and core (A1(C)) of the
 269 nodule were analyzed and resulted in a very similar REE pattern but the calculated Ce and Pr anomalies shift
 270 towards a more positive Ce and more negative Pr anomaly from rim to core (Fig. 4e).

271 Of the samples where calcite replaced anhydrite, there are three samples (C11, C5 & C4) with REE patterns unlike
 272 the rest (Fig. 4c), all collected from drill core FC15-28 (2153.9 m, 2202.6 m and 2202.8 m TVD SS; Fig. 1c). They
 273 show a convex upward increase in LREE up to europium and a continuous decrease in HREEY with positive
 274 europium and yttrium anomalies (Fig. 4c). The Y/Ho ratios in these samples are 37, 41 and 49 and they do not have
 275 a distinct Cerium anomaly (Bau and Dulski, 1996) (Fig. 4e). The total concentration in REE in these samples is 4, 9
 276 and 11 ppm.

277 4.3 Stable isotopes

278 The stable isotope data is presented in the order of the paragenetic sequence. Three quartz samples consisting of a
 279 siliceous band (sample C3), a silicified breccia (sample Q1) and a quartz nodule (sample Q2) have a very similar
 280 oxygen isotopic signature of 28.1‰, 27.5‰ and 28.1‰ V-SMOW respectively (Table 1). The original limestone
 281 samples (L1(1), L1(2), C7(L) and A4(L)) comprises a mean $\delta^{13}\text{C}$ value of 2.0‰ V-PDB (1.5 to 3‰, n=4) and a
 282 mean $\delta^{18}\text{O}$ value of -7.9‰ V-PDB (-8.9 to -7.3‰, n=4), where n is the number of different samples analyzed except
 283 for sample L1 where the same sample was sampled twice (Table 1 & Fig. 5). The dolomite host rock samples (D1,

284 D2, D3 and D4) have a mean $\delta^{13}\text{C}$ value of 3.8‰ V-PDB (2.0 to 7.2‰, n=4) and $\delta^{18}\text{O}$ value of -2.1‰ V-PDB (-3.3
 285 to 0.0‰, n=4) (Table 1 & Fig. 5). The coarse-grained fracture-filling calcite samples (A4, C12, C6, A5 and LB2)
 286 have a positive mean $\delta^{13}\text{C}$ value of 1.4‰ V-PDB (0.7 to 2.4‰, n=5) and a negative mean $\delta^{18}\text{O}$ value of -8.4‰ V-
 287 PDB (-10.0 to -6.6‰, n=5) (Table 1 & Fig. 5). The saddle dolomite sample (A4(D)) has $\delta^{13}\text{C}$ and $\delta^{18}\text{O}$ values of
 288 1.9‰ V-PDB and -9.8‰ V-PDB respectively (Table 1 & Fig. 5). The calcite that replaced anhydrite samples (Table
 289 1) have a distinct negative carbon isotope composition of -11.6‰ V-PDB (-18.3 to -5.9‰, n=18) and an oxygen
 290 isotope composition of -11.6‰ V-PDB (-13.7 to -8.6‰, n=18). Sample A1 shows a higher $\delta^{13}\text{C}$ and lower $\delta^{18}\text{O}$
 291 value in the rim (sample A1(F)) than in the core (sample A1(C); Table 1 & Fig. 5).
 292 The pyrite samples seem to form two groups based on their sulphur isotopic signatures ($\delta^{34}\text{S}$) (Fig. 6a). One sample
 293 group (samples P4, P5(1), P5(2) and P11) exhibits a very negative mean $\delta^{34}\text{S}$ value of -25.9‰ (-33.2 to -19.5‰,
 294 n=4), whilst the remaining samples show positive $\delta^{34}\text{S}$ values with a mean of 6.9‰ (3.6 to 9.5‰, n=8) (Table 1).
 295 Two native sulphur samples (samples S1 and S2) have $\delta^{34}\text{S}$ values of -0.2‰ and 10.7‰ (Table 1 & Fig. 6a). The
 296 isotopic values of the fracture-filling CAS are $\delta^{34}\text{S}$ 15.3‰ and $\delta^{18}\text{O}$ 14.7‰ (Fig. 6b). The mean $\delta^{34}\text{S}$ value of the
 297 nodular CAS samples is 20.2‰ (15.3 to 22.3‰, n=11) and the associated $\delta^{18}\text{O}$ value is 17.3‰ (15.1 to 18.6‰,
 298 n=10) (Fig. 6b). The nodular CAS sample A1 shows a simultaneous increase in $\delta^{34}\text{S}$ and $\delta^{18}\text{O}$ values from rim to
 299 core (Fig. 6b).
 300 The CAS sulphur and oxygen isotopes exhibit two systematic linear trends when compared to each other and to
 301 carbon isotopes. The first trend is from lighter CAS $\delta^{18}\text{O}$ and $\delta^{34}\text{S}$ values to heavier ones in the fracture-filling
 302 calcite and nodular calcite samples (Fig. 6b). This trend has a coefficient of determination (R^2) of 0.83. In the second
 303 trend the nodular CAS samples vary from heavier $\delta^{13}\text{C}$ and lighter $\delta^{18}\text{O}$ and $\delta^{34}\text{S}$ values to lighter $\delta^{13}\text{C}$ and heavier
 304 $\delta^{18}\text{O}$ and $\delta^{34}\text{S}$ values (Fig. 6c & d). The observed trend is not linear and exhibits two different slopes (Fig. 6c & d).
 305 At first the CAS $\delta^{18}\text{O}$ and $\delta^{34}\text{S}$ increase gradually with decreasing $\delta^{13}\text{C}$ values but then the trend changes and $\delta^{13}\text{C}$
 306 values decrease with almost no change in CAS $\delta^{18}\text{O}$ and $\delta^{34}\text{S}$ values. The gradual change of $\delta^{13}\text{C}$ with CAS $\delta^{18}\text{O}$ and
 307 $\delta^{34}\text{S}$ values exhibits a R^2 of 0.96 and 0.76, respectively.

308 4.4 Fluid inclusions

309 Homogenisation temperatures (T_h) and freezing point depressions (T_m ice) of primary and secondary aqueous fluid
 310 inclusion assemblages hosted in micro-spar, quartz, fracture-filling calcite, fluorite, saddle dolomite and calcite that
 311 replaced anhydrite were measured in core samples from three wells (Fig. 7, Table 3).
 312 The analyzed quartz samples tend to have an euhedral crystal habit with a cloudy inclusion-rich core followed by a
 313 clear, relatively inclusion-free rim. In drill core FC13-10, T_h values of primary inclusions decrease from ~140-145
 314 °C in the cloudy core to ~115 °C at the boundary with the clear rim, indicating a temperature drop during quartz
 315 precipitation (Fig. 7). In FC15-28 fluorite-hosted primary fluid inclusions have T_h values of 105 to 115 °C, very
 316 similar to the temperatures in the outer growth zone of euhedral quartz. This suggests these phases may have formed
 317 close in time to each other. Primary fluid inclusions in calcite that replaced anhydrite have T_h of ≥ 175 °C (Table 3).
 318 Following crystallization of all phases, secondary fluid inclusion assemblages hosted in quartz, fluorite, and calcite
 319 indicate that fluids with a maximum temperature of ~210-215 °C migrated through the Madison Formation (Table 3
 320 & Fig. 7).
 321 Fluid inclusion salinities are generally significantly higher than seawater (Table 3). Primary inclusions in quartz and
 322 fluorite almost ubiquitously have salinities in excess of 21 weight % (NaCl equivalent). However, primary
 323 inclusions in calcite that replaced anhydrite and secondary inclusions in quartz and calcite that replaced anhydrite
 324 tend to have lower salinities. The final ice melting temperature of many of these later inclusions were difficult to
 325 measure due to a high concentration of $\text{CH}_4 \pm \text{CO}_2 \pm \text{H}_2\text{S}$ dissolved in the water resulting in clathrate formation upon
 326 freezing. Thus, some salinity values represent a maximum, rather than absolute value (see Table 3). Regardless,
 327 these salinities are lower than the salinities found in primary inclusions in quartz and fluorite (Table 3).

328 5 Data interpretation

329 5.1. Paragenetic sequence

330 The observed limestone texture and composition are consistent with the interpretation that the Madison Formation
 331 was deposited in a shallow water, subtidal setting (Gutschick & Sandberg, 1983; Sando, 1976). Dolomitisation has
 332 been interpreted to have occurred during early burial by seepage and reflux of hypersaline brines (Moore, 1995;
 333 Moore, 2001; Smith, 1991; Sonnenfeld, 1996a) and the observations made in this study are consistent with that

334 interpretation. On the basis that quartz replaces the dolomitic breccia and is enveloped by fracture-filling calcite,
335 quartz and silica are interpreted to have formed before the fracture-filling calcite. The small variation in oxygen
336 isotopic values from the silica phases suggests that precipitation occurred from a single fluid in a narrow time range.
337 The decreasing fluid inclusion homogenisation temperatures from core to rim in the quartz replaced anhydrite
338 nodule suggests precipitation from a hydrothermal fluid that cooled from 165 °C to potentially ambient temperatures
339 of 115 °C (Table 3). Subsequently, some micro-fractures developed and were occluded by fracture-filling calcite,
340 most likely from the same fluid as the quartz.

341
342 Fluorite inclusions were observed alongside anhydrite in quartz replacing anhydrite and in calcite that replaced
343 anhydrite. This suggests that the first fluorite phase was evaporitic in origin, in agreement with observations in
344 dolomitic rocks of the Florida aquifer (Cook et al., 1985). The source for the second fluorite phase, occurring as a
345 single vein and postdating the fracture-filling calcite, is likely external in origin. The fluid inclusion homogenisation
346 temperature of this vein fits with the interpretation of a brine cooling to ambient temperature of 105 - 115 °C and
347 precipitating quartz, fracture-filling calcite and then fluorite. The saddle dolomite postdates the fracture-filling
348 calcite since the dolomite crystals enclose some fracture-filling calcite crystals.

349
350 The last precipitating phase of calcite is that which replaced anhydrite. The observation of large crystals in the centre
351 of the nodules suggests that the anhydrite was replaced from rim towards the core which is consistent with
352 observations elsewhere (Alonso-Zarza et al., 2002; Hesse, 1989; Milliken, 1979; Worden & Smalgeoley, 1996).
353 Pyrite and minor amounts of sphalerite are precipitated along grain boundaries and enclosed within calcite crystals
354 that replaced anhydrite, implying contemporaneous formation. Solid bitumen and native sulphur precipitated either
355 contemporaneously or later than the calcite that replaced anhydrite since they are precipitated in between calcite
356 crystals.

357 5.2. Evidence for TSR

358 Evidence for in situ sulphate reduction at the LaBarge Field comes from the identification of various reduced
359 sulphur phases including native sulphur, pyrite, sphalerite and H₂S. In addition, other known by-products of sulphur
360 reduction were observed, including calcite that replaced anhydrite and solid bitumen (Kelemen et al., 2010; Kendall,
361 2001; King et al., 2014; Machel, 2001) which are related in time and space to the reduced sulphur phases.

362
363 Depending on the reaction temperature, sulphate reduction is usually caused by either bacterial or thermochemical
364 sulphate reduction (Machel, 2001 and references therein). To explain the presence of solid bitumen, oil had to be
365 present in the reservoir at some time prior to or concomitant with sulphate reduction. Oil is reported to have
366 migrated into the Madison Formation around 76-84 Ma ago (Roberts et al., 2005). At that time the formation
367 temperature was approximately 90-120 °C based on the thermal history reported by (Roberts et al., 2005). During
368 and after oil migration into the LaBarge field, the formation temperature was too high (>80 °C) for bacterial
369 sulphate reduction (BSR) (Machel, 2001 and references therein). Fluid inclusion data infer precipitation
370 temperatures of >175 °C for the calcite that replaced anhydrite and therefore also exclude BSR as a sulphate
371 reduction mechanism (Table 3). In addition, the gas composition at the LaBarge Field is more analogous to other
372 systems with ≥5-10% H₂S that is reported to be a product of TSR rather than BSR (Machel, 2001 and references
373 therein).

374 375 5.3. Rare earth elements

376
377 Calcite REEY patterns are influenced by the fluid composition and physicochemical precipitation conditions (Bau &
378 Möller, 1992). In sedimentary carbonate reservoirs the REEY pattern of the precursor limestone can be preserved
379 during diagenesis and dolomitization under low and moderate fluid-rock ratios (Banner et al., 1988). The fracture-
380 filling calcite samples have similar REEY patterns to seawater, with characteristic Ce and Y/Ho anomalies (Fig. 4a).
381 Their lower HREE abundance compared to seawater could arise from the decreasing compatibility of HREE that are
382 incorporated in diagenetic calcite, compared to LREE (Fig. 4a) (Tanaka & Kawabe, 2006; Zhong & Mucci, 1995).
383 The cerium anomaly calculated by the method of Bau and Dulski (1996) can indicate the oxidation state of the fluid
384 at the time of the calcite precipitation (Fig. 4e). Under oxic conditions cerium is oxidised to the immobile ion Ce⁴⁺
385 and hence the fluid will have a depleted cerium concentration. Alternatively the cerium anomaly can be derived
386 from the host rock during fluid-rock interaction. The REEY pattern and the cerium anomaly of the fracture-filling

387 calcite are likely inherited from the host rock probably through recrystallization of the micro-spar. Further support
 388 for this comes from oxygen isotopic data which will be discussed in the next subsection.

389
 390 The majority of calcite that replaced anhydrite samples have flat REEY pattern with Y/Ho ratios mainly in the range
 391 of seawater, a low to non-existent cerium anomaly and an order of magnitude lower concentration of REE than
 392 fracture filling calcite samples. The Y/Ho ratios suggest the fluid inherited the Y/Ho during replacement of
 393 anhydrite. The two Y/Ho ratios that are slightly above and below seawater values are harder to explain. The
 394 calculated cerium anomalies in these samples lie on a trend from negative Ce and positive Pr anomalies to no Ce and
 395 Pr anomalies, which indicates a trend towards a more reducing environment (Fig. 4e). This trend is also seen in
 396 sample A1, which shows more reducing conditions from the rim (A1(F)) to the core (A1(C)) of the sample.

397
 398 Additionally, there are three anhydrite replacing calcite phases (sample C4, C5 and C11) that show convex upward
 399 shaped REEY patterns with positive Eu and Y/Ho anomalies. Convex upward shaped REE patterns have been
 400 documented for many hydrothermal waters and carbonates that formed from acidic crustal fluids (Bau & Möller,
 401 1992; Hecht et al., 1999; Lüders et al., 1993; Michard, 1989; Möller, 1983; Ohr et al., 1994). In these studies, the
 402 fluids most likely originated from interactions with pelitic metasediments or gneisses under acidic conditions
 403 whereby apatite is mobilized (Hecht et al., 1999; Möller et al., 1997; Ohr et al., 1994). Yttrium and holmium exhibit
 404 a similar geochemical behaviour and therefore remain coupled during many geochemical processes (Bau & Dulski,
 405 1999; Jochum et al., 1986). Volcanic and detrital rocks exhibit chondritic Y/Ho ratios of 28 (Bau, 1996; Jochum et
 406 al., 1986) and therefore crustal fluids exhibit chondritic rather than superchondritic Y/Ho ratios (>28). The
 407 superchondritic values of the three dissimilar calcites that replaced anhydrite, however, could have formed during
 408 fluid advection, whereby Y is less adsorbed than any other trivalent REE (Möller, 1997; Möller et al., 2004). An
 409 excess of Eu relative to the neighbouring REE is generated during water rock interaction at temperatures >200 °C
 410 (Bau, 1991; Sverjensky, 1984). Under these conditions the Eu ions are reduced to Eu^{2+} which are less susceptible to
 411 sorption and preferentially transported in the fluid (Bau & Möller, 1992; Bau, 1991). The Eu anomaly remains even
 412 if the fluids migrate into a cooler, oxidizing region where Eu^{3+} is incorporated into the precipitating calcite (Bau et
 413 al., 2010). Eu^{3+} is preferentially incorporated into calcite due to its smaller ionic radius compared to Eu^{2+} (Lüders et
 414 al., 1993). The production of a positive Eu anomaly without high temperature water-rock interaction is unlikely due
 415 to the low oxygen fugacity required to reduce Eu^{2+} at low temperature (Bau & Möller, 1992; Bau, 1991), except
 416 when the H_2S concentration exceeds the SO_4^{2-} concentration in the fluid (Lüders et al., 1993; Möller, 1983). Positive
 417 Eu anomalies could even be produced in closed system basins if burial temperatures exceed 200°C and fluid rock
 418 interaction occurs (Jiang et al., 2015). In the LaBarge Field the maximum estimated burial depth of the base of the
 419 Madison Formation was 6600 m. When interpreted in the context of a known geothermal gradient of 28.8 °C/km
 420 and surface temperatures of 25°C, this yields a maximum burial temperature of 215 °C (Fig. 2) (Roberts et al.,
 421 2005). However, uncertainties associated with estimates of exhumation and erosion are sufficient for this
 422 temperature to be within error of the 200 °C required for an Eu anomaly in a closed system. Alternatively, it is
 423 possible that the observed positive Eu anomalies are related to a hydrothermal fluid. There is no distinct cerium
 424 anomaly measured in these samples, which indicates precipitation under reducing conditions. In conclusion, these
 425 three samples indicate a different fluid at a different time in the system.

426 5.4 Carbon and oxygen isotopes and fluid temperatures

427 The limestone host rock at the LaBarge Field has a carbon and oxygen isotopic signature consistent with other
 428 measurements of the Mississippian Madison Formation in Wyoming (e.g. ($\delta^{13}\text{C}$ 0.5 to 6.5‰, $\delta^{18}\text{O}$ -5.5 to -1‰)
 429 Budai and Cummings, 1987 ; ($\delta^{13}\text{C}$ -3 to 7‰, $\delta^{18}\text{O}$ -9 to 3‰) Katz et al., 2006). The Mississippian seawater oxygen
 430 isotopic composition has been estimated to be between -1‰ and -5.3‰ V-SMOW (Came et al., 2007; Veizer et al.,
 431 2000; Wallmann, 2004) which equates to a limestone of -3.7‰ to -7.8‰ V-PDB at a typical precipitation
 432 temperature of 25 °C (Kim & O'Neil, 1997). The oxygen isotope of the limestone at the LaBarge Field (-7.3‰ to -
 433 8.9‰ V-PDB) is lighter than these estimates and therefore another process likely modified the original composition.
 434 The oxygen isotopic composition of the fracture-filling calcite, however, overlaps with those of the limestone, which
 435 suggests that the micro-spar recrystallised during the precipitation of the fracture-filling calcite and hence lowered
 436 the limestone's oxygen isotope value (Fig. 5). This is in agreement with the seawater like REE composition of the
 437 fracture-filling calcite inherited from interaction with the micro-spar. The carbon and oxygen isotopes of the
 438 dolomite host rock are consistent with previous observations of the Madison Formation where the dolomite was
 439 interpreted to have formed as early diagenetic phase by reflux of hypersaline brines (e.g. ($\delta^{13}\text{C}$ 0.5 to 4.1‰, $\delta^{18}\text{O}$ -3.2

440 to 1‰) Budai et al., 1984; Smith, 1991; ($\delta^{13}\text{C}$ -1 to 6.9‰, $\delta^{18}\text{O}$ -8.5 to 3‰) Smith et al., 2004; ($\delta^{13}\text{C}$ -2.9 to 7.1‰,
441 $\delta^{18}\text{O}$ -8.9 to 6.3‰) Katz, 2008).

442 To integrate the fluid origins of the different phases the fluid compositions were calculated based on the mineral
443 $\delta^{18}\text{O}$ composition combined with the fluid inclusion microthermometry data. The anhydrite-replacement quartz
444 (sample Q2), with an oxygen isotope composition of 28.1‰, is in equilibrium with a fluid ranging from 12.2 to
445 8.5‰ V-SMOW at the inferred precipitation temperatures from primary fluid inclusion homogenisation
446 temperatures in quartz from 145 - 115 °C (Clayton et al., 1972). Since the fluid inclusion homogenisation
447 temperatures in quartz decrease from core to rim and exhibits a high salinity, the quartz likely precipitated from an
448 external fluid with an isotopically heavy composition, such as a basinal brine that was mobilized through laramide
449 deformation.

450 As discussed above, fracture-filling calcite precipitation postdates quartz precipitation but predates the precipitation
451 of fluorite in the vein. Given that there are independent constraints on the precipitation temperature of quartz at 145-
452 115 °C and a well defined paragenesis, it can be assumed that the fracture filling calcite precipitated at a similar
453 temperature to that of the quartz. If the fracture filling calcite did precipitate at a temperature of 115 °C, it would
454 have precipitated from a fluid with an oxygen isotope composition of 7.6‰ V-SMOW (Kim & O'Neil, 1997) based
455 on the average measured isotopic signature of the four samples. This is close to the lowest value calculated from the
456 last precipitating quartz sample, and suggests that these phases precipitated from a common pore fluid. Furthermore,
457 the similar carbon isotopic composition of the fracture-filling calcite to that of the Madison Formation host rock
458 suggests that this calcite precipitated from a fluid in equilibrium with the host rock with moderate to low fluid-rock
459 ratios (Sheppard & Schwarz, 1970).

460 The carbon isotopic value of the saddle dolomite (1.9‰) suggests that it also precipitated from a fluid in equilibrium
461 with the host rock because of the overlap in their isotopic signatures (Table 1). The saddle dolomite postdates the
462 fracture-filling calcite, with primary fluid inclusion homogenization temperatures demonstrating that this
463 precipitated at 145-160 °C. A fluid in equilibrium with the oxygen isotopic value of the saddle dolomite at these
464 temperatures would have a heavy isotopic composition, between 7.9 and 9.6‰ V-SMOW (Kim & O'Neil, 1997;
465 Sheppard & Schwarz, 1970). These values are within the range of those estimated for the precipitation of quartz and
466 fracture filling calcite, again indicative of precipitation from a common pore fluid at increasingly elevated
467 temperatures.

468 The carbon and oxygen isotopes of the calcite that replaced anhydrite form a distinct group. The carbon isotopes of
469 the calcite that replaced anhydrite samples are strikingly clustered at <-5‰ and are all at least 5‰ lighter than the
470 host rock (Fig. 5). This large difference between the host rock and the calcite that replaced anhydrite indicates that
471 there must have been a source of isotopically light carbon in the fluid when this calcite phase precipitated. Potential
472 sources of isotopically light carbon at the temperatures at which calcite-replacement of anhydrite took place (175-
473 200 °C based on fluid inclusion homogenization temperatures) include hydrocarbons or carbon dioxide. The oxygen
474 isotope values of these samples cluster between average host rock values and much lower values of up to -13.7‰ V-
475 PDB. The low oxygen isotopic values could have originated from either precipitation at increasingly elevated
476 temperatures or precipitation from an isotopically light fluid. The most common, volumetrically abundant,
477 isotopically light diagenetic fluid is meteoric water but given that this precipitation occurred at burial depths of
478 several kilometres this is highly unlikely. Using the average oxygen isotopic composition and the fluid inclusion
479 homogenisation temperatures (175-200 °C) of anhydrite-replacement calcite, the oxygen isotopic composition of the
480 fluid from which this cement precipitated was estimated to be 10.7 to 12.9‰ (V-SMOW) (Kim & O'Neil, 1997). It
481 is unclear from the stable isotopes alone if this isotopically heavy fluid could either be an external crustal fluid or the
482 result of fluid rock interaction of indigenous formation water at high temperatures.

484 5.5. CAS stable isotope fractionation in TSR

485 The CAS isotopic signature of the fracture-filling calcites are interpreted to record the sulphate present in the
486 reservoir prior to TSR as their values lie in the range of Mississippian seawater of $\delta^{34}\text{S}$ 14-21.5‰ and $\delta^{18}\text{O}$ 14-18‰
487 (Claypool et al., 1980; Kampschulte et al., 2001; Kampschulte & Strauss, 2004). This suggests that the
488 Mississippian anhydrites were controlling the aqueous sulphate prior to TSR (Fig. 6b). The nodular CAS sample
489 with the lowest $\delta^{34}\text{S}$ and $\delta^{18}\text{O}$ isotopic values (sample C10) exhibits an isotopic composition very close to the

490 fracture-filling calcite sample (sample C12) and supports the previous inference that the Mississippian sulphate
491 source dominated when the TSR process started. An additional influx of dissolved sulphate from the overlying
492 Permian Phosphoria Formation characterised by much lower sulphur and oxygen isotopic values has been suggested
493 previously (King et al., 2014), but this is not supported by the CAS data presented here (Fig. 6b).

494
495 The variation and correlation between sulphur and oxygen isotopes in CAS can be caused by primary (sedimentary)
496 or secondary diagenetic processes. In the first case, the isotopic signature would be indicative of evaporite
497 precipitation prior to burial. However, the fractionation is negligible between seawater sulphate and the precipitating
498 anhydrite (Burdett et al., 1989; Kampschulte et al., 2001; Kampschulte & Strauss, 2004; Newton et al., 2004) and
499 hence no isotopic difference would be expected between the different samples. Support for this comes from the
500 observation that only a few anhydrite micro-inclusions are present in the calcite that replaced anhydrite. Hence most
501 of the CAS is interpreted to be lattice bound sulphate that was incorporated into the precipitating calcite.
502 Consequently the isotopic composition of CAS represents the sulphate composition of the fluid at the time of calcite
503 replacement. As such, there is no plausible explanation for a primary origin of the isotopic co-variation in the CAS
504 (Fig. 6b).

505
506 The second possibility for the correlation of the oxygen and sulphur isotopes is a secondary process such as BSR or
507 TSR. In redox reactions such as these, the isotopic values of the source material increases successively with
508 continuous reaction progress due to the preferential reaction of the lighter isotopes (a normal isotope effect),
509 enriching the residual source material in the heavier isotope. In BSR systems, increasing isotopic values with
510 increasing depth have been observed and related to increasing reaction progression (Aharon & Fu, 2000, 2003;
511 Antler et al., 2013; Böttcher et al., 1998; Fritz et al., 1989; Strebel et al., 1990). In these systems, a linear correlation
512 between $\delta^{34}\text{S}$ and $\delta^{18}\text{O}$ isotopes has been attributed to kinetic fractionation of oxygen and sulphur isotopes during
513 the same reaction step (Aharon & Fu, 2000, 2003; Antler et al., 2013). Kinetic fractionation of sulphur isotopes
514 during TSR has also been observed experimentally (Cross et al., 2004; Kiyosu, 1980; Kiyosu & Krouse, 1993, 1990;
515 Meshoulam et al., 2016). In the LaBarge Field, TSR is the dominant sulphate reduction process that fractionated the
516 sulphate. The slope of the correlation between the CAS oxygen and sulphur isotopes ($\delta^{18}\text{O}/\delta^{34}\text{S}$) is 0.53, which
517 means that the sulphur fractionation is almost double that of oxygen (Fig. 6b).

518
519 Further isotopic variation caused by TSR can be found among the products of the redox reaction. The calcite that
520 replaced anhydrite exhibits a trend from heavier $\delta^{13}\text{C}$ and lighter $\delta^{18}\text{O}$ and $\delta^{34}\text{S}$ values to lighter $\delta^{13}\text{C}$ and heavier
521 $\delta^{18}\text{O}$ and $\delta^{34}\text{S}$ values (Fig. 6c & d). In the first segment (upper arrow in Fig. 6c & d) the decrease in $\delta^{13}\text{C}$ values
522 could arise from mixing of the carbon already present in the pore water (as HCO_3^-) with an isotopically light carbon
523 (as $\text{CO}_2(\text{g})$) produced as a by-product of TSR. This is in agreement with the simultaneous increase in CAS $\delta^{18}\text{O}$ and
524 $\delta^{34}\text{S}$ that arose as a result of the progressive distillation of these isotopes during TSR. A similar trend has been
525 observed in other TSR reservoirs where decreasing $\delta^{13}\text{C}$ values in calcite have been attributed to an increased extent
526 of anhydrite reaction (Machel et al., 1995; Worden & Smalgeoley, 1996) and decreasing $\delta^{13}\text{C}$ values in water have
527 been associated with the progress of TSR (Wynn et al., 2010). Sample A1 which has been analysed in the rim and
528 core is in agreement with this observed trend and records an evolving fluid composition at two different times. The
529 carbon and CAS isotopic data of sample A1(C) plot at the intersection of the two observed trends (circled sample in
530 Fig. 6c & d). The growth of the large calcite crystal in this sample reflects slower precipitation near equilibrium and
531 therefore could represent the termination of the TSR process in this system.

532
533 In the second segment (lower arrow in Fig. 6c & d) the continuous decrease in $\delta^{13}\text{C}$ is not accompanied by a
534 continuous increase in CAS $\delta^{18}\text{O}$ and $\delta^{34}\text{S}$. This shift in isotope evolution was attributed to be associated with fluid
535 mixing with an external carbon source that is not connected to the TSR process (Fig. 6c & d). The addition of
536 isotopically light or hot CO_2 will change the carbon isotopic composition of the fluid but will not have an influence
537 on the sulphate isotopic composition of the fluid since the isotope exchange reaction between dissolved sulphate and
538 water is extremely slow (Llyod, 1967). The $\delta^{13}\text{C}$ of the $\text{CO}_2(\text{g})$ present today in the LaBarge Field has an average
539 value of -5.2‰ (-5.45 to -5.02‰ , $n=8$) (Frost, 2011) and is in equilibrium with the isotopically lightest calcites at
540 210°C (Clark & Fritz, 1997; Romanek et al., 1992; Sheppard & Schwarz, 1970). This segment might record a
541 formation fluid no longer influenced by TSR but instead by the influx of CO_2 . There is not enough resolution or data
542 to unambiguously determine whether the hydrothermal CO_2 arrived prior to, during or after TSR, although it seems
543 unlikely that it entered prior or during TSR because of the apparent equilibrium precipitation of the large crystals
544 that precede the onset of precipitation of isotopically lighter calcite (Fig. 6c & d).

545

546 Other products of TSR in the LaBarge Field are H₂S and the metal sulphides that potentially precipitated from it. In
 547 a closed system the kinetic fractionation of TSR can be described as a Rayleigh type fractionation process (Kiyosu
 548 & Krouse, 1990). Starting with an initial sulphate isotopic composition of 15.3‰ and a H₂S(g) in equilibrium with
 549 the pyrite with the lowest positive δ³⁴S value of +3.6‰ (Ohmoto & Rye, 1979) the temperature at which the
 550 fractionation factor matches these numbers can be inferred. The fractionation factor Py-SO₄²⁻ is -11.7 (Kiyosu &
 551 Krouse, 1990; Ohmoto & Rye, 1979) at a temperature of 155 °C. The successive increase in δ³⁴S of subsequent
 552 pyrite phases could then be explained by formation from an increasingly isotopically enriched H₂S. The
 553 accumulated H₂S would reach the observed δ³⁴S value of 10‰ (King et al., 2014) after over 80% of the sulphate is
 554 consumed. In the temperature range of TSR (>100 °C) (Machel, 2001), the fractionation between sulphate and
 555 sulphide is not large enough to form isotopically negative pyrites which have been identified in two of the cores
 556 (Kiyosu & Krouse, 1990). Even though there is no petrographic indication or other evidence for bacterial sulphate
 557 reduction these isotopically negative pyrites have likely formed diagenetically below 80 °C (Machel, 2001 and
 558 references therein).
 559

560 6 Discussion

561 6.1 Sulphur cycling and duration of TSR

562 Sulphur cycling in the LaBarge Field can be traced by estimating source and sink material affected by TSR. The
 563 gross rock volume of the LaBarge reservoir is estimated to be 1400 km³ based on a reservoir map (Stilwell 1989)
 564 (Fig. 1b). The average porosity is 9% (Huang et al., 2007), which yields a total pore volume of 126 km³. An
 565 estimated volume of former anhydrite nodules in the drill cores of 0.2 vol% would equate to 2.55 x 10⁹ m³ or 5.6 x
 566 10¹³ mol in the reservoir. The amount of CO₂ is estimated to be 3.15 x 10⁺¹² m³ STP (DeBuin, 1991; Lynds 2010).
 567 Based on an assumed CO₂-H₂S ratio of 1:13 (gas composition of 65% CO₂ and 5% H₂S) (Huang et al., 2007) and
 568 this CO₂ volume, the H₂S gas volume is calculated to be 2.4 x 10¹¹ m³, or 9.8 x 10¹² mol. The amount of anhydrite
 569 therefore exceeds the amount of H₂S by a factor 6. The overall TSR reaction (CaSO₄ + HC -> H₂S + CaCO₃/CO₂ +
 570 solid bitumen + altered HC+H₂O) would yield 1 mol of H₂S for each mol of reacted anhydrite (Goldhaber & Orr,
 571 1995; Machel, 1987b; Orr, 1974). Therefore it is likely that the H₂S found in the Madison Formation in the LaBarge
 572 Field has been produced from the dissolved local anhydrite without an external sulphate source even though no
 573 primary anhydrite is left. It is proposed that dissolved sulphate remained abundant in the fluid since calcite that
 574 precipitated after TSR also contains sulphate and present day fluids hold 10000 mg/L SO₄²⁻ (Blondes et al., 2014).
 575 The discrepancy between the amount of anhydrite and H₂S could be associated with spatial heterogeneity in the
 576 anhydrite content of the Madison Formation, with H₂S migration out of the reservoir or another reason for anhydrite
 577 dissolution unrelated to sulphate reduction. Alternatively, it could be explained by sulphide precipitation, which
 578 consumes 2 moles of H₂S for each mole of pyrite precipitated. The amount of pyrite estimated through logging of
 579 the three drill cores is approximately 10 ppm and equates to 4 x 10⁺⁴ mol and results in 8 x 10⁺⁴ moles of H₂S
 580 consumed. This suggests that sulphide precipitation played a subordinate role in reducing the amount of H₂S in the
 581 reservoir, compared to the 9.8 x 10⁺¹² moles of H₂S present today.
 582 The kinetics and duration of TSR are not well understood (Machel, 2001). Due to the extensive fractionation in
 583 δ³⁴S_{sulphate} the rate limiting step was likely the reduction rather than sulphate dissolution (Fig. 6b; Meshoulam et al.,
 584 2016). Goldhaber and Orr, (1995) estimated a rate for the reduction step of 10⁻⁶ moles of sulphate per litre per year
 585 for high H₂S systems at 150 °C. In the LaBarge Field the amount of reacted sulphate is at least the equivalent of the
 586 total amount of H₂S (9.8 x 10¹² mol). Assuming a total pore space of 1.26*10¹⁰ m³ (Huang et al., 2007; Stilwell,
 587 1989) filled with water, the pore fluid would have had a sulphate concentration of 0.8 mol/L. This concentration
 588 would take approximately 80 ka to react (Goldhaber & Orr, 1995). The reaction time could increase if there was a
 589 higher initial sulphate concentration or decrease if the TSR process occurred at a higher temperature than 150 °C.
 590 Aqueous fluid inclusions in calcite that replaced anhydrite (>175 °C) provide good evidence that temperatures
 591 exceeded 150 °C (i.e. up to 200 °C; Fig. 7) and as such, this time represents an upper limit on the likely duration of
 592 TSR in the LaBarge Field.

593 6.2 Fluid sources and timing of TSR

594 The composition of the main fluid phases that circulated in the reservoir are recorded in the fracture-filling calcite,
 595 the solid bitumen and the calcite that replaced anhydrite (Fig. 8). The fracture-filling calcite cement most likely

596 precipitated from a saline brine following quartz precipitation. This is supported by the quartz fluid inclusion
597 homogenisation temperatures showing decreasing temperatures from the core of the crystals to the rim (Fig. 7).
598 During or following fracture-filling calcite precipitation, the reservoir was charged with oil from the overlying
599 Phosphoria Formation (Johnson, 2005)(Fig. 8). The calcite that replaced anhydrite formed after the influx of oil and
600 the start of TSR, indicated by the low carbon isotopic values, the more reducing conditions indicated by the lack of
601 negative cerium anomalies, and the solid bitumen co-/post-precipitation. TSR progressed in the reservoir and altered
602 the fluid composition as suggested by the increase in CAS isotopic values with decreasing carbon isotopic values. At
603 some point, TSR ceased and the fluid composition remained stable and close to equilibrium for some time, reflected
604 in the development of large crystals in the core of some calcite that replaced anhydrite nodules. There is no direct
605 evidence of the limiting factor that caused the TSR process in the LaBarge Field to cease, but a likely explanation is
606 that the heavy hydrocarbons were totally consumed and the reaction could not progress with methane as the only
607 organic source left in the reservoir (Amrani et al., 2008; Machel, 2001 and references therein). The excess of a
608 reaction product, however, could also have halted the reaction. This raises the possibility of a pause between TSR
609 and the influx of the CO₂, and suggests that the influx of CO₂ did not influence the progression of TSR in the
610 LaBarge Field.

611
612 Following TSR, hydrothermal CO₂ is interpreted to have flooded the reservoir, reflected in the decreasing carbon
613 isotopic composition with limited variation in the CAS isotopic composition in some of the calcite that replaced
614 anhydrite samples (Fig. 6 c & d). The gaseous CO₂ that currently occupies the reservoir is in equilibrium with the
615 lightest carbon isotope signatures in calcite at a temperature of 210 °C (Clark & Fritz, 1997; Romanek et al., 1992;
616 Sheppard & Schwarz, 1970). Indeed, the observed positive Eu anomalies and the convex upward shaped REE
617 pattern in three of the calcite that replaced anhydrite samples indicate the presence of an acidic hydrothermal fluid
618 and are therefore probably related to the external CO₂ influx. The three calcite phases that replaced anhydrite
619 samples from drill core FC15-28 are the deepest samples (2150 to 2200 m TVD SS) and are located next to a
620 basement-involved reverse fault (Kraig et al., 1987), hence the fluid might have entered the reservoir along this fault
621 (Stilwell, 1989). This interpretation is supported by the observation that CO₂ concentration increases towards the
622 base of the reservoir and towards this fault (Stilwell, 1989). The source of the CO₂, however, remains uncertain; the
623 CO₂ has a δ¹³C and a ³He/CO₂ ratio in mantle range (Frost, 2011; Merrill et al., 2014), yet there is no evidence that a
624 magmatic fluid could have produced the convex upward shaped REE pattern with a positive Eu anomaly (Banks et
625 al., 1994) unless it interacted with meta-sediments along the flow path.

626

627 **7 Conclusion**

628 (1) Mineralogical and petrographical observations, along with the burial history and fluid inclusion data, argue for
629 in-situ TSR in the LaBarge Field.

630 (2) It has been shown that sulphate sulphur and oxygen isotopes co-fractionated during the TSR process. This
631 indicates a fractionation in the same reaction step during which the sulphur isotopes fractionate almost twice the
632 amount of the oxygen isotopes. The CAS isotopic data also reveal that a single Mississippian sulphate source was
633 involved in TSR.

634 (3) The progression of the TSR reaction is illustrated by the co-fractionation in CAS isotopes to higher values,
635 accompanied by a decreasing δ¹³C value. The end of TSR is marked by the precipitation of large calcite crystals in
636 the core of some calcite that replaced anhydrite nodules.

637 (4) The limiting factor for TSR is likely the exhaustion of heavy hydrocarbons since mass balance calculations and
638 present day pore-fluid analyses suggest that dissolved sulphate occurred in excess.

639 (5) The approximate length of TSR is 80 ka, based on a reaction rate from Goldhaber and Orr (1995) and the
640 assumption of a reaction step limiting system due to the extensive sulphate fractionation (Meshoulam et al., 2016).
641 Depending on the reservoir age, dating techniques could also provide useful constraints about the duration of the
642 TSR process at the LaBarge Field.

643 (6) An influx of an external source of CO₂ after the cessation of TSR is marked by a trend of decreasing δ¹³C with
644 limited changes in CAS isotopic values. This suggests that the influx of CO₂ did not influence the TSR process. A
645 possible entry point for the CO₂ could be located along the reverse fault on the west side of the field based on
646 observations from REE data. The source of the CO₂ remains controversial, however, future Nd isotopic
647 measurements could help to distinguish between a mantle and a crustal origin of CO₂ and lead to a better
648 understanding of the timing of the CO₂ influx and narrow the age and temperature range of the TSR process.

649 (7) Altogether, it has been shown that the combination of petrography, REE, fluid inclusion and stable isotope
 650 measurements can be useful to disentangle the fluid history of a large reservoir and could help to predict the
 651 occurrence and magnitude of TSR elsewhere.

652 **Acknowledgments, Samples, and Data**

653 Thanks to Thomas Becker at ExxonMobil for discussions on the burial history of the LaBarge Field. We would like
 654 to thank Peter Wynn at Lancaster University for discussions about the CAS methodology and Dave Hughes at
 655 Lancaster University for helping with the stable isotope measurements. Further we acknowledge Alison Mc Donald
 656 from the Scottish Universities Environmental research centre for her support with the pyrite isotopic analysis. We
 657 also thank Paul Lythgoe at the University of Manchester for conducting the rare earth element measurements. This
 658 work was supported by the University of Manchester and Lancaster University. The data used can be found in the
 659 tables 1-3.

660 **References**

- 661 Aharon, P., & Fu, B. (2000). Microbial sulfate reduction rates and sulfur and oxygen isotope
 662 fractionations at oil and gas seeps in deepwater Gulf of Mexico. *Geochimica et*
 663 *Cosmochimica Acta*, 64(2), 233–246. [https://doi.org/10.1016/S0016-7037\(99\)00292-6](https://doi.org/10.1016/S0016-7037(99)00292-6)
- 664 Aharon, P., & Fu, B. (2003). Sulfur and oxygen isotopes of coeval sulfate–sulfide in pore fluids
 665 of cold seep sediments with sharp redox gradients. *Chemical Geology*, 195(1–4), 201–218.
 666 [https://doi.org/http://dx.doi.org/10.1016/S0009-2541\(02\)00395-9](https://doi.org/http://dx.doi.org/10.1016/S0009-2541(02)00395-9)
- 667 Allis, R., Chidsey, T., Gwynn, W., Morgan, C., White, S., Adams, M., & Moore, J. (2001).
 668 Natural CO₂ reservoirs on the Colorado Plateau and southern Rocky Mountains: Candidates
 669 for CO₂ sequestration. *Proceedings of the First National Conference on Carbon*
 670 *Sequestration*, 14–17.
- 671 Alonso-Zarza, A. M., Sánchez-Moya, Y., Bustillo, M. A., Sopen, A., & Delgado, A. (2002).
 672 Silicification and dolomitization of anhydrite nodules in argillaceous terrestrial deposits: An
 673 example of meteoric-dominated diagenesis from the Triassic of central Spain.
 674 *Sedimentology*, 49(2), 303–317. <https://doi.org/10.1046/j.1365-3091.2002.00442.x>
- 675 Amrani, A., Zhang, T., Ma, Q., Ellis, G. S., & Tang, Y. (2008). The role of labile sulfur
 676 compounds in thermochemical sulfate reduction. *Geochimica et Cosmochimica Acta*,
 677 72(12), 2960–2972.
- 678 Anderson, G. M., & Thom, J. (2008). The role of thermochemical sulfate reduction in the origin
 679 of Mississippi Valley-type deposits. II. Carbonate–sulfide relationships. *Geofluids*, 8(1),
 680 27–34.
- 681 Antler, G., Turchyn, A. V., Rennie, V., Herut, B., & Sivan, O. (2013). Coupled sulfur and oxygen
 682 isotope insight into bacterial sulfate reduction in the natural environment. *Geochimica et*
 683 *Cosmochimica Acta*, 118, 98–117. <https://doi.org/10.1016/j.gca.2013.05.005>
- 684 Banks, D. A., Yardley, B. W. D., Campbell, A. R., & Jarvis, K. E. (1994). REE composition of
 685 an aqueous magmatic fluid: A fluid inclusion study from the Capitan Pluton, New Mexico,
 686 U.S.A. *Chemical Geology*, 113(3–4), 259–272. [https://doi.org/10.1016/0009-](https://doi.org/10.1016/0009-2541(94)90070-1)
 687 [2541\(94\)90070-1](https://doi.org/10.1016/0009-2541(94)90070-1)
- 688 Banner, J. L., Hanson, G. N., & Meyers, W. J. (1988). Rare earth element and Nd isotopic

- 689 variations in regionally extensive dolomites from the Burlington-Keokuk Formation
690 (Mississippian): Implications for REE mobility during carbonate diagenesis. *Journal of*
691 *Sedimentary Research*, 58(3), 415–432.
- 692 Bau, M. (1991). Rare-earth element mobility during hydrothermal and metamorphic fluid-rock
693 interaction and the significance of the oxidation state of europium. *Chemical Geology*,
694 93(3), 219–230.
- 695 Bau, M. (1996). Controls on the fractionation of isovalent trace elements in magmatic and
696 aqueous systems: evidence from Y/Ho, Zr/Hf, and lanthanide tetrad effect. *Contributions to*
697 *Mineralogy and Petrology*, 123(3), 323–333. <https://doi.org/10.1007/s004100050159>
- 698 Bau, M., & Dulski, P. (1995). Comparative study of yttrium and rare-earth element behaviours in
699 fluorine-rich hydrothermal fluids. *Contributions to Mineralogy and Petrology*, 119(2), 213–
700 223. <https://doi.org/10.1007/BF00307282>
- 701 Bau, M., & Dulski, P. (1996). Distribution of yttrium and rare-earth elements in the Penge and
702 Kuruman iron-formations, Transvaal Supergroup, South Africa. *Precambrian Research*,
703 79(1), 37–55.
- 704 Bau, M., & Dulski, P. (1999). Comparing yttrium and rare earths in hydrothermal fluids from the
705 Mid-Atlantic Ridge: implications for Y and REE behaviour during near-vent mixing and for
706 the Y/Ho ratio of Proterozoic seawater. *Chemical Geology*, 155(1), 77–90.
- 707 Bau, M., & Möller, P. (1992). Rare earth element fractionation in metamorphogenic
708 hydrothermal calcite, magnesite and siderite. *Mineralogy and Petrology*, 45(3–4), 231–246.
- 709 Bau, M., Balan, S., Schmidt, K., & Koschinsky, A. (2010). Rare earth elements in mussel shells
710 of the Mytilidae family as tracers for hidden and fossil high-temperature hydrothermal
711 systems. *Earth and Planetary Science Letters*, 299(3), 310–316.
- 712 Becker, T. P., & Lynds, R. (2012). A geologic deconstruction of one of the world's largest
713 natural accumulations of CO₂, Moxa arch, southwestern Wyoming. *AAPG Bulletin*, 96(9),
714 1643–1664. <https://doi.org/10.1306/01251211089>
- 715 Bickle, M., Kampman, N., & Wigley, M. (2013). Natural analogues. In DePaolo, D.J., et Al.,
716 Eds., *Geochemistry of Geologic CO₂ Sequestration: Reviews in Mineralogy and*
717 *Geochemistry*, 77(1), 15–71.
- 718 Biehl, B. C., Reuning, L., Schoenherr, J., Lüders, V., & Kukla, P. A. (2016). Impacts of
719 hydrothermal dolomitization and thermochemical sulfate reduction on secondary porosity
720 creation in deeply buried carbonates: A case study from the Lower Saxony Basin, northwest
721 Germany. *AAPG Bulletin*, 100(4), 597–621.
- 722 Bildstein, O., Worden, R. H., & Brosse, E. (2001). Assessment of anhydrite dissolution as the
723 rate-limiting step during thermochemical sulfate reduction. *Chemical Geology*, 176(1–4),
724 173–189. [https://doi.org/http://dx.doi.org/10.1016/S0009-2541\(00\)00398-3](https://doi.org/http://dx.doi.org/10.1016/S0009-2541(00)00398-3)
- 725 Blackstone, D. L. (1979). *Geometry of the Prospect-Darby and La Barge faults at their junction*
726 *with the La Barge platform, Lincoln and Sublette Counties, Wyoming*. Geological Survey of

727 Wyoming.

728 Blondes, M. S., Gans, K. D., Thordsen, J. J., Reidy, M. E., Thomas, B., Engle, M. A., et al.
729 (2014). U.S. Geological Survey National Produced Waters Geochemical Database v2.1
730 (PROVISIONAL). *Energy Resources Program - Produced Waters, 1*. Retrieved from
731 [http://semanticcommunity.info/@api/deki/files/35790/USGS_Produced_Waters_Database_v](http://semanticcommunity.info/@api/deki/files/35790/USGS_Produced_Waters_Database_v2.1_Documentation.pdf)
732 [2.1_Documentation.pdf](http://semanticcommunity.info/@api/deki/files/35790/USGS_Produced_Waters_Database_v2.1_Documentation.pdf)

733 Böttcher, M. E., Oelschläger, B., Höpner, T., Brumsack, H. J., & Rullkötter, J. (1998). Sulfate
734 reduction related to the early diagenetic degradation of organic matter and “black spot”
735 formation in tidal sandflats of the German Wadden Sea (southern North Sea): Stable isotope
736 (^{13}C , ^{34}S , ^{18}O) and other geochemical results. *Organic Geochemistry*, 29(5–7–7 pt 2),
737 1517–1530. [https://doi.org/10.1016/S0146-6380\(98\)00124-7](https://doi.org/10.1016/S0146-6380(98)00124-7)

738 De Bruin, R. H. (2001). Carbon dioxide in Wyoming, information pamphlet 8: Wyoming
739 Geological Survey. *Laramie, Wyoming*, 1–11.

740 Budai, C., & Cummings, M. (1987). A depositional model of the Antelope Coal Field, Powder
741 River Basin, Wyoming. *Journal of Sedimentary Petrology*, 57:30-38(1), 30–38.
742 <https://doi.org/10.1306/212F8A94-2B24-11D7-8648000102C1865D>

743 Budai, J. (1985). Evidence for rapid fluid migration during deformation, Madison Group,
744 Wyoming and Utah Overthrust Belt. *Rocky Mountain Carbonate Reservoirs — A Core*
745 *Workshop [Golden, CO, August 10-11, 1985]*, 377–407. Retrieved from
746 [http://archives.datapages.com/data/sepm_sp/cw7/Evidence_of_Rapid_Fluid_Migration_duri](http://archives.datapages.com/data/sepm_sp/cw7/Evidence_of_Rapid_Fluid_Migration_during.pdf)
747 [ng.pdf](http://archives.datapages.com/data/sepm_sp/cw7/Evidence_of_Rapid_Fluid_Migration_during.pdf)

748 Budai, J., Lohmann, K. C., & Owen, R. M. (1984). Burial dedolomite in the Mississippian
749 Madison Limestone, Wyoming and Utah thrust belt. *Journal of Sedimentary Petrology*,
750 54(1), 276–288. <https://doi.org/10.1306/212F83FF-2B24-11D7-8648000102C1865D>

751 Buoniconti, M. R. (2008). *The evolution of the carbonate shelf margins and fill of the Antler*
752 *Foreland Basin by prograding Mississippian carbonates, Northern US Rockies*. *Open*
753 *Access Dissertations*. Retrieved from
754 http://scholarlyrepository.miami.edu/oa_dissertations/330

755 Burdett, J. W., Arthur, M. A., & Richardson, M. (1989). A Neogene seawater sulfur isotope age
756 curve from calcareous pelagic microfossils. *Earth and Planetary Science Letters*, 94(3),
757 189–198.

758 Cai, C., Hu, W., & Worden, R. H. (2001). Thermochemical sulphate reduction in Cambro–
759 Ordovician carbonates in Central Tarim. *Marine and Petroleum Geology*, 18(6), 729–741.
760 [https://doi.org/http://dx.doi.org/10.1016/S0264-8172\(01\)00028-9](https://doi.org/http://dx.doi.org/10.1016/S0264-8172(01)00028-9)

761 Cai, C., Worden, R. H., Bottrell, S. H., Wang, L., & Yang, C. (2003). Thermochemical sulphate
762 reduction and the generation of hydrogen sulphide and thiols (mercaptans) in Triassic
763 carbonate reservoirs from the Sichuan Basin, China. *Chemical Geology*, 202(1–2), 39–57.
764 [https://doi.org/http://dx.doi.org/10.1016/S0009-2541\(03\)00209-2](https://doi.org/http://dx.doi.org/10.1016/S0009-2541(03)00209-2)

- 765 Cai, C., Xie, Z., Worden, R. H., Hu, G., Wang, L., & He, H. (2004). Methane-dominated
766 thermochemical sulphate reduction in the Triassic Feixianguan Formation East Sichuan
767 Basin, China: towards prediction of fatal H₂S concentrations. *Marine and Petroleum*
768 *Geology*, 21(10), 1265–1279.
769 <https://doi.org/http://dx.doi.org/10.1016/j.marpetgeo.2004.09.003>
- 770 Cai, C., Zhang, C., Cai, L., Wu, G., Jiang, L., Xu, Z., et al. (2009). Origins of Palaeozoic oils in
771 the Tarim Basin: Evidence from sulfur isotopes and biomarkers. *Chemical Geology*, 268(3),
772 197–210. <https://doi.org/http://dx.doi.org/10.1016/j.chemgeo.2009.08.012>
- 773 Cai, C., Li, K., Zhu, Y., Xiang, L., Jiang, L., Cai, X., & Cai, L. (2010). TSR origin of sulfur in
774 Permian and Triassic reservoir bitumen, East Sichuan Basin, China. *Organic Geochemistry*,
775 41(9), 871–878.
- 776 Cai, C., Zhang, C., He, H., & Tang, Y. (2013). Carbon isotope fractionation during methane-
777 dominated TSR in East Sichuan Basin gasfields, China: A review. *Marine and Petroleum*
778 *Geology*, 48, 100–110.
- 779 Cai, C., Amrani, A., Worden, R. H., Xiao, Q., Wang, T., Gvirtzman, Z., et al. (2016). Sulfur
780 isotopic compositions of individual organosulfur compounds and their genetic links in the
781 Lower Paleozoic petroleum pools of the Tarim Basin, NW China. *Geochimica et*
782 *Cosmochimica Acta*, 182, 88–108.
783 <https://doi.org/http://dx.doi.org/10.1016/j.gca.2016.02.036>
- 784 Came, R. E., Eiler, J. M., Veizer, J., Azmy, K., Brand, U., & Weidman, C. R. (2007). Coupling
785 of surface temperatures and atmospheric CO₂ concentrations during the Palaeozoic era.
786 *Nature*, 449(7159), 198–201. Retrieved from <http://dx.doi.org/10.1038/nature06085>
- 787 Campbell-Stone, E., Lynds, R., Frost, C., Becker, T. P., & Diem, B. (2011). The Wyoming
788 Carbon Underground Storage Project: Geologic characterization of the Moxa Arch and
789 Rock Springs Uplift. *Energy Procedia*, 4, 4656–4663.
790 <https://doi.org/10.1016/j.egypro.2011.02.426>
- 791 Clark, I. D., & Fritz, P. (1997). *Environmental isotopes in hydrogeology*. CRC press.
- 792 Claypool, G. E., & Mancini, E. A. (1989). Geochemical relationships of petroleum in Mesozoic
793 reservoirs to carbonate source rocks of Jurassic Smackover Formation, southwestern
794 Alabama. *AAPG Bulletin*, 73(7), 904–924.
- 795 Claypool, G. E., Holser, W. T., Kaplan, I. R., Sakai, H., & Zak, I. (1980). The age curves of
796 sulfur and oxygen isotopes in marine sulfate and their mutual interpretation. *Chemical*
797 *Geology*, 28, 199–260.
- 798 Clayton, R. N., & Mayeda, T. K. (1963). The use of bromine pentafluoride in the extraction of
799 oxygen from oxides and silicates for isotopic analysis. *Geochimica et Cosmochimica Acta*,
800 27(1), 43–52. [https://doi.org/http://dx.doi.org/10.1016/0016-7037\(63\)90071-1](https://doi.org/http://dx.doi.org/10.1016/0016-7037(63)90071-1)
- 801 Clayton, R. N., O’Neil, J. R., & Mayeda, T. K. (1972). Oxygen isotope exchange between quartz
802 and water. *Journal of Geophysical Research*, 77(17), 3057–3067.

- 803 Cook, D. J., Randazzo, A. F., & Sprinkle, C. L. (1985). Authigenic fluorite in dolomitic rocks of
804 the Floridan aquifer. *Geology*, *13*(6), 390–391. [https://doi.org/10.1130/0091-](https://doi.org/10.1130/0091-7613(1985)13<390:AFIDRO>2.0.CO;2)
805 [7613\(1985\)13<390:AFIDRO>2.0.CO;2](https://doi.org/10.1130/0091-7613(1985)13<390:AFIDRO>2.0.CO;2)
- 806 Cross, M. M., Manning, D. A. C., Bottrell, S. H., & Worden, R. H. (2004). Thermochemical
807 sulphate reduction (TSR): experimental determination of reaction kinetics and implications
808 of the observed reaction rates for petroleum reservoirs. *Organic Geochemistry*, *35*(4), 393–
809 404.
- 810 Ding, K., Li, S., Yue, C., & Zhong, N. (2008). Simulation experiments on the reaction system of
811 CH₄–MgSO₄–H₂O. *Chin. Sci. Bull*, *53*, 1071–1078.
- 812 Ding, K., Li, S., & Yue, C. (2009). Simulation experiments on thermochemical origin of high
813 H₂S in natural gas. *Energy Sources, Part A: Recovery, Utilization, and Environmental*
814 *Effects*, *32*(3), 246–255.
- 815 Dixon, J. S. (1982). Regional structural synthesis, Wyoming salient of Western Overthrust belt.
816 *American Association of Petroleum Geologists Bulletin*, *66*(10), 1560–1580.
817 <https://doi.org/10.1306/03B5A98A-16D1-11D7-8645000102C1865D>
- 818 Dulski, P. (1994). Interferences of oxide, hydroxide and chloride analyte species in the
819 determination of rare earth elements in geological samples by inductively coupled plasma-
820 mass spectrometry. *Fresenius' Journal of Analytical Chemistry*, *350*(4), 194–203.
821 <https://doi.org/10.1007/bf00322470>
- 822 Fritz, P., Basharmal, G. M., Drimmie, R. J., Ibsen, J., & Qureshi, R. M. (1989). Oxygen isotope
823 exchange between sulphate and water during bacterial reduction of sulphate. *Chemical*
824 *Geology: Isotope Geoscience Section*, *79*(2), 99–105. [https://doi.org/10.1016/0168-](https://doi.org/10.1016/0168-9622(89)90012-2)
825 [9622\(89\)90012-2](https://doi.org/10.1016/0168-9622(89)90012-2)
- 826 Frost, C. (2011). *Carbon Sequestration Monitoring Activities*. UNT Digital Library. Retrieved
827 from <http://digital.library.unt.edu/ark:/67531/metadc836030/>
- 828 Glezakou, V.-A., McGrail, B. P., & Schaef, H. T. (2012). Molecular interactions of SO₂ with
829 carbonate minerals under co-sequestration conditions: A combined experimental and
830 theoretical study. *Geochimica et Cosmochimica Acta*, *92*, 265–274.
831 <https://doi.org/http://dx.doi.org/10.1016/j.gca.2012.06.015>
- 832 Goldhaber, M., & Orr, W. (1995). Kinetic controls on thermochemical sulfate reduction as a
833 source of sedimentary H₂S. *ACS Symposium Series*, *612*, 412–425.
- 834 Goldstein, R. H., & Reynolds, T. J. (1994). Systematics of fluid inclusions in diagenetic
835 minerals: SEPM Short Course 31. *Society for Sedimentary Geology*, 199.
- 836 De Groot, P. A. (2008). *Handbook of Stable Isotope Analytical Techniques* (Vol. 2). Elsevier.
- 837 Gutschick, R. C., & Sandberg, C. A. (1983). Mississippian continental margins of the
838 conterminous United States. *The Shelfbreak: Critical Interface on Continental Margins*, 79–
839 96. Retrieved from [https://www.scopus.com/inward/record.uri?eid=2-s2.0-](https://www.scopus.com/inward/record.uri?eid=2-s2.0-0021061102&partnerID=40&md5=3c4fb6fb8ea09e723d912cca2217811c)
840 [0021061102&partnerID=40&md5=3c4fb6fb8ea09e723d912cca2217811c](https://www.scopus.com/inward/record.uri?eid=2-s2.0-0021061102&partnerID=40&md5=3c4fb6fb8ea09e723d912cca2217811c)

- 841 Hao, F., Zhang, X., Wang, C., Li, P., Guo, T., Zou, H., et al. (2015). The fate of CO₂ derived
842 from thermochemical sulfate reduction (TSR) and effect of TSR on carbonate porosity and
843 permeability, Sichuan Basin, China. *Earth-Science Reviews*, 141(0), 154–177.
844 <https://doi.org/http://dx.doi.org/10.1016/j.earscirev.2014.12.001>
- 845 Hecht, L., Freiberger, R., Gilg, H. A., Grundmann, G., & Kostitsyn, Y. A. (1999). Rare earth
846 element and isotope (C, O, Sr) characteristics of hydrothermal carbonates: genetic
847 implications for dolomite-hosted talc mineralization at Göpfersgrün (Fichtelgebirge,
848 Germany). *Chemical Geology*, 155(1), 115–130.
- 849 Hesse, R. (1989). Silica diagenesis: origin of inorganic and replacement cherts. *Earth Science*
850 *Reviews*, 26(C), 253–284. [https://doi.org/10.1016/0012-8252\(89\)90024-X](https://doi.org/10.1016/0012-8252(89)90024-X)
- 851 Heydari, E., & Moore, C. H. (1989). Burial diagenesis and thermochemical sulfate reduction,
852 Smackover Formation, southeastern Mississippi salt basin. *Geology*, 17(12), 1080–1084.
- 853 Huang, N. S., Aho, G. E., Baker, B. H., Matthews, T. R., & Pottorf, R. J. (2007). *Integrated*
854 *reservoir modeling to maximize the value of a large sour-gas field with high concentrations*
855 *of inerts: International Petroleum Technology Conference Paper 11202. IPTC conference*
856 *in Dubai, UAE.*
- 857 Jarvis, K. E., Gray, A. L., & McCurdy, E. (1989). Avoidance of spectral interference on
858 europium in inductively coupled plasma mass-spectrometry by sensitive measurement of
859 the doubly charged ion. *Journal of Analytical Atomic Spectrometry*, 4(8), 743–747.
860 <https://doi.org/10.1039/ja9890400743>
- 861 Jenden, P. D., Titley, P. A., & Worden, R. H. (2015). Enrichment of nitrogen and ¹³C of
862 methane in natural gases from the Khuff Formation, Saudi Arabia, caused by
863 thermochemical sulfate reduction. *Organic Geochemistry*, 82, 54–68.
864 <https://doi.org/10.1016/j.orggeochem.2015.02.008>
- 865 Jiang, L., Worden, R. H., & Cai, C. F. (2014). Thermochemical sulfate reduction and fluid
866 evolution of the Lower Triassic Feixianguan Formation sour gas reservoirs, northeast
867 Sichuan Basin, China. *AAPG Bulletin*, 98(5), 947–973.
- 868 Jiang, L., Cai, C., Worden, R. H., Li, K., Xiang, L., Chu, X., et al. (2015). Rare earth element
869 and yttrium (REY) geochemistry in carbonate reservoirs during deep burial diagenesis:
870 Implications for REY mobility during thermochemical sulfate reduction. *Chemical*
871 *Geology*, 415, 87–101.
- 872 Jochum, K. P., Seufert, H. M., Spettel, B., & Palme, H. (1986). The solar-system abundances of
873 Nb, Ta, and Y, and the relative abundances of refractory lithophile elements in
874 differentiated planetary bodies. *Geochimica et Cosmochimica Acta*, 50(6), 1173–1183.
- 875 Johnson, E. A. (2005). Geologic assessment of undiscovered oil and gas resources in the
876 Phosphoria Total Petroleum System, southwestern Wyoming province, Wyoming,
877 Colorado, and Utah. *US Geological Survey Southwestern Wyoming Province Assessment*
878 *Team, Eds., Petroleum Systems and Geologic Assessment of Oil and Gas in the*
879 *Southwestern Wyoming Province, Wyoming, Colorado, and Utah: US Geological Survey*

880 *Digital Data Series DDS-69-D.*

- 881 Kampschulte, A., & Strauss, H. (2004). The sulfur isotopic evolution of Phanerozoic seawater
882 based on the analysis of structurally substituted sulfate in carbonates. *Chemical Geology*,
883 *204*(3–4), 255–286. <https://doi.org/http://dx.doi.org/10.1016/j.chemgeo.2003.11.013>
- 884 Kampschulte, A., Bruckschen, P., & Strauss, H. (2001). The sulphur isotopic composition of
885 trace sulphates in Carboniferous brachiopods: implications for coeval seawater, correlation
886 with other geochemical cycles and isotope stratigraphy. *Chemical Geology*, *175*(1), 149–
887 173.
- 888 Kaszuba, J. P., Navarre-Sitchler, A., Thyne, G., Chopping, C., & Meuzelaar, T. (2011).
889 Supercritical carbon dioxide and sulfur in the Madison Limestone: A natural analog in
890 southwest Wyoming for geologic carbon–sulfur co-sequestration. *Earth and Planetary*
891 *Science Letters*, *309*(1–2), 131–140.
892 <https://doi.org/http://dx.doi.org/10.1016/j.epsl.2011.06.033>
- 893 Katz, D. A. (2008). Early and Late Diagenetic Processes of Mississippian Carbonates , Northern
894 U . S . Rockies. *Open Access Dissertations, Paper 154*. Retrieved from
895 http://scholarlyrepository.miami.edu/oa_dissertations/154/
- 896 Katz, D. A., Eberli, G. P., Swart, P. K., & Smith, L. B. (2006). Tectonic-hydrothermal
897 brecciation associated with calcite precipitation and permeability destruction in
898 Mississippian carbonate reservoirs, Montana and Wyoming. *AAPG Bulletin*, *90*(11), 1803–
899 1841. <https://doi.org/10.1306/03200605072>
- 900 Katz, D. A., Buoniconti, M. R., Montañez, I. P., Swart, P. K., Eberli, G. P., & Smith, L. B.
901 (2007). Timing and local perturbations to the carbon pool in the lower Mississippian
902 Madison Limestone, Montana and Wyoming. *Palaeogeography, Palaeoclimatology*,
903 *Palaeoecology*, *256*(3), 231–253.
- 904 Kelemen, S. R., Walters, C. C., Kwiatek, P. J., Freund, H., Afeworki, M., Sansone, M., et al.
905 (2010). Characterization of solid bitumens originating from thermal chemical alteration and
906 thermochemical sulfate reduction. *Geochimica et Cosmochimica Acta*, *74*(18), 5305–5332.
- 907 Kendall, A. C. (2001). Late diagenetic calcitization of anhydrite from the Mississippian of
908 Saskatchewan, western Canada. *Sedimentology*, *48*(1), 29–55.
909 <https://doi.org/10.1111/j.1365-3091.2001.00350.x>
- 910 Kim, S.-T., & O’Neil, J. R. (1997). Equilibrium and nonequilibrium oxygen isotope effects in
911 synthetic carbonates. *Geochimica et Cosmochimica Acta*, *61*(16), 3461–3475.
- 912 King, H. E., Walters, C. C., Horn, W. C., Zimmer, M., Heines, M. M., Lamberti, W. A., et al.
913 (2014). Sulfur isotope analysis of bitumen and pyrite associated with thermal sulfate
914 reduction in reservoir carbonates at the Big Piney–La Barge production complex.
915 *Geochimica et Cosmochimica Acta*, *134*, 210–220.
- 916 Kiyosu, Y. (1980). Chemical reduction and sulfur-isotope effects of sulfate by organic matter
917 under hydrothermal conditions. *Chemical Geology*, *30*(1–2), 47–56.

- 918 [https://doi.org/10.1016/0009-2541\(80\)90115-1](https://doi.org/10.1016/0009-2541(80)90115-1)
- 919 Kiyosu, Y., & Krouse, H. R. (1993). Thermochemical reduction and sulfur isotopic behavior of
920 sulfate by acetic acid in the presence of native sulfur. *Geochemical Journal*, 27(1), 49–57.
921 <https://doi.org/10.2343/geochemj.27.49>
- 922 Kiyosu, Y., & Krouse, R. H. (1990). The role of organic and acid the in the sulfur abiogenic
923 isotope reduction effect. *Geochemical Journal*, 24, 21–27. Retrieved from
924 <http://jlc.jst.go.jp/DN/JALC/00004729259?from=Google>
- 925 Knauss, K. G., Johnson, J. W., & Steefel, C. I. (2005). Evaluation of the impact of CO₂, co-
926 contaminant gas, aqueous fluid and reservoir rock interactions on the geologic sequestration
927 of CO₂. *Chemical Geology*, 217(3–4), 339–350.
928 <https://doi.org/http://dx.doi.org/10.1016/j.chemgeo.2004.12.017>
- 929 Kraig, D. H., Wiltschko, D. V., & Spang, J. H. (1987). Interaction of basement uplift and thin-
930 skinned thrusting, Moxa arch and the Western Overthrust Belt, Wyoming: A hypothesis.
931 *Geological Society of America Bulletin*, 99, 654.
- 932 Leng, M., Barnker, P., Greenwood, P., Roberts, N., & Reed, J. (2001). Oxygen isotope analysis
933 of diatom silica and authigenic calcite from Lake Pinarbasi, Turkey. *Journal of*
934 *Paleolimnology*, 25(3), 343–349. <https://doi.org/10.1023/a:1011169832093>
- 935 Leng, M. J., & Sloane, H. J. (2008). Combined oxygen and silicon isotope analysis of biogenic
936 silica. *Journal of Quaternary Science*, 23(4), 313–319.
- 937 Liu, Q. Y., Worden, R. H., Jin, Z. J., Liu, W. H., Li, J., Gao, B., et al. (2013). TSR versus non-
938 TSR processes and their impact on gas geochemistry and carbon stable isotopes in
939 Carboniferous, Permian and Lower Triassic marine carbonate gas reservoirs in the Eastern
940 Sichuan Basin, China. *Geochimica et Cosmochimica Acta*, 100, 96–115.
- 941 Liu, Q. Y., Worden, R. H., Jin, Z. J., Liu, W. H., Li, J., Gao, B., et al. (2014). Thermochemical
942 sulphate reduction (TSR) versus maturation and their effects on hydrogen stable isotopes of
943 very dry alkane gases. *Geochimica et Cosmochimica Acta*, 137, 208–220.
- 944 Llyod, R. M. (1967). Oxygen-18 composition of oceanic sulfate. *Science (New York, N.Y.)*,
945 156(3779), 1228–1231. <https://doi.org/10.1126/science.156.3779.1228>
- 946 Lüders, V., Möller, P., & Dulski, P. (1993). REE fractionation in carbonates and fluorite.
947 *Monograph Series on Mineral Deposits*, 30(9), 133–150.
- 948 Lynds, R., Campbell-Stone, E., Becker, T. P., & Frost, C. D. (2010). Stratigraphic evaluation of
949 reservoir and seal in a natural CO₂ field: Lower Paleozoic, Moxa Arch, southwest
950 Wyoming. *Rocky Mountain Geology*, 45(2), 113–132.
951 <https://doi.org/10.2113/gsrocky.45.2.113>
- 952 Machel, H. G. (1987a). Saddle dolomite as a by-product of chemical compaction and
953 thermochemical sulfate reduction. *Geology*, 15(10), 936–940. [https://doi.org/10.1130/0091-7613\(1987\)15<936:SDAABO>2.0.CO;2](https://doi.org/10.1130/0091-7613(1987)15<936:SDAABO>2.0.CO;2)

- 955 Machel, H. G. (1987b). Some aspects of diagenetic sulphate-hydrocarbon redox reactions.
956 *Geological Society, London, Special Publications*, 36(1), 15–28.
- 957 Machel, H. G. (2001). Bacterial and thermochemical sulfate reduction in diagenetic settings—
958 old and new insights. *Sedimentary Geology*, 140(1), 143–175.
- 959 Machel, H. G., Krouse, H. R., & Sassen, R. (1995). Products and distinguishing criteria of
960 bacterial and thermochemical sulfate reduction. *Applied Geochemistry*, 10(4), 373–389.
- 961 Marenco, P. J., Corsetti, F. A., Hammond, D. E., Kaufman, A. J., & Bottjer, D. J. (2008).
962 Oxidation of pyrite during extraction of carbonate associated sulfate. *Chemical Geology*,
963 247(1–2), 124–132. <https://doi.org/10.1016/j.chemgeo.2007.10.006>
- 964 McLennan, S. M. (1989). Rare earth elements in sedimentary rocks; influence of provenance and
965 sedimentary processes. *Reviews in Mineralogy and Geochemistry*, 21(1), 169–200.
- 966 Merrill, M. D., Hunt, A. G., & Lohr, C. D. (2014). Noble gas geochemistry investigation of high
967 CO₂ natural gas at the LaBarge Platform, Wyoming, USA. *Energy Procedia*, 63, 4186–
968 4190. <https://doi.org/10.1016/j.egypro.2014.11.451>
- 969 Meshoulam, A., Ellis, G. S., Said Ahmad, W., Deev, A., Sessions, A. L., Tang, Y., et al. (2016).
970 Study of thermochemical sulfate reduction mechanism using compound specific sulfur
971 isotope analysis. *Geochimica et Cosmochimica Acta*, 188, 73–92.
972 <https://doi.org/http://dx.doi.org/10.1016/j.gca.2016.05.026>
- 973 Michard, A. (1989). Rare earth element systematics in hydrothermal fluids. *Geochimica et*
974 *Cosmochimica Acta*, 53(3), 745–750.
- 975 Middleton, G. V. (1961). Evaporite Solution Breccias from the Mississippian of Southwest
976 Montana. *Journal of Sedimentary Petrology*, 31(2), 189–195.
977 <https://doi.org/10.1306/74D70B32-2B21-11D7-8648000102C1865D>
- 978 Milliken, K. Lou. (1979). The silicified evaporite syndrome - two aspects of silicification history
979 of former evaporite nodules from southern kentucky and northern tennessee. *JOURNAL OF*
980 *SEDIMENTARY PETROLOGY*, 49(1), 245–256. [https://doi.org/10.1306/212F7707-2B24-](https://doi.org/10.1306/212F7707-2B24-11D7-8648000102C1865D)
981 [11D7-8648000102C1865D](https://doi.org/10.1306/212F7707-2B24-11D7-8648000102C1865D)
- 982 Mitra, A., Elderfield, H., & Greaves, M. J. (1994). Rare earth elements in submarine
983 hydrothermal fluids and plumes from the Mid-Atlantic Ridge. *Marine Chemistry*, 46(3),
984 217–235.
- 985 Möller, P. (1983). Lanthanoids as a Geochemical Probe and Problems in Lanthanoid
986 Geochemistry Distribution and Behaviour of Lanthanoids in Non-Magmatic-Phases. In S. P.
987 Sinha (Ed.), *Systematics and the Properties of the Lanthanides* (pp. 561–616). Dordrecht:
988 Springer Netherlands. https://doi.org/10.1007/978-94-009-7175-2_13
- 989 Möller, P. (1997). Rare earth element and yttrium fractionation caused by fluid migration.
990 *Journal of Geosciences*, 42(3), 43. Retrieved from
991 <http://www.jgeosci.org/content/JCGS.602/abstract>

- 992 Möller, P., Stober, I., & Dulski, P. (1997). Seltenerdelement-, Yttrium-Gehalte und Bleiisotope
993 in Thermal- und Mineralwässern des Schwarzwaldes. *Grundwasser*, 2(3), 118–132.
994 <https://doi.org/10.1007/s767-1997-8533-0>
- 995 Möller, P., Dulski, P., Savascin, Y., & Conrad, M. (2004). Rare earth elements, yttrium and Pb
996 isotope ratios in thermal spring and well waters of West Anatolia, Turkey: a hydrochemical
997 study of their origin. *Chemical Geology*, 206(1–2), 97–118.
998 <https://doi.org/http://dx.doi.org/10.1016/j.chemgeo.2004.01.009>
- 999 Moore, C. H. (1995). Gas production from a super-deep dolomite reservoir. In *Madden field,*
1000 *Wind River Basin, Wyoming, USA: AAPG Hedberg Conference on the Carbonate*
1001 *Reservoirs of the World: Problems, Solutions and Strategies for the Future, Pau, France,*
1002 *session (Vol. 3).*
- 1003 Moore, C. H. (2001). *Carbonate Reservoirs: Porosity, Evolution & Diagenesis in a Sequence*
1004 *Stratigraphic Framework (Vol. 55).* Elsevier.
- 1005 Nance, W. B., & Taylor, S. R. (1976). Rare earth element patterns and crustal evolution—I.
1006 Australian post-Archean sedimentary rocks. *Geochimica et Cosmochimica Acta*, 40(12),
1007 1539–1551.
- 1008 Newton, R. J., Pevitt, E. L., Wignall, P. B., & Bottrell, S. H. (2004). Large shifts in the isotopic
1009 composition of seawater sulphate across the Permo–Triassic boundary in northern Italy.
1010 *Earth and Planetary Science Letters*, 218(3), 331–345.
- 1011 Nozaki, Y., Zhang, J., & Amakawa, H. (1997). The fractionation between Y and Ho in the
1012 marine environment. *Earth and Planetary Science Letters*, 148(1), 329–340.
1013 [https://doi.org/10.1016/S0012-821X\(97\)00034-4](https://doi.org/10.1016/S0012-821X(97)00034-4)
- 1014 Ohmoto, H., & Rye, R. O. (1979). *Isotopes of sulfur and carbon. Geochemistry of Hydrothermal*
1015 *Ore Deposits (Barnes, HL, ed.).* John Wiley & Sons Inc., New York.
- 1016 Ohr, M., Halliday, A. N., & Peacor, D. R. (1994). Mobility and fractionation of rare earth
1017 elements in argillaceous sediments: implications for dating diagenesis and low-grade
1018 metamorphism. *Geochimica et Cosmochimica Acta*, 58(1), 289–312.
- 1019 Orr, W. L. (1974). Changes in sulfur content and isotopic ratios of sulfur during petroleum
1020 maturation--study of Big Horn basin Paleozoic oils. *AAPG Bulletin*, 58(11), 2295–2318.
- 1021 Pearce, J. K., Golab, A., Dawson, G. K. W., Knuefing, L., Goodwin, C., & Golding, S. D.
1022 (2016). Mineralogical controls on porosity and water chemistry during O₂-SO₂-CO₂
1023 reaction of CO₂ storage reservoir and cap-rock core. *Applied Geochemistry*, 75, 152–168.
1024 <https://doi.org/http://dx.doi.org/10.1016/j.apgeochem.2016.11.002>
- 1025 Piqué, À., Canals, À., Disnar, J. R., & Grandia, F. (2009). In situ thermochemical sulfate
1026 reduction during ore formation at the Ixaspe Zn-(Pb) MVT occurrence (Basque-Cantabrian
1027 basin, Northern Spain). *Geologica Acta*, 7(4), 431–449.
1028 <https://doi.org/10.1344/105.000001448>
- 1029 Powell, T. G., & MacQueen, R. W. (1984). Precipitation of sulfide ores and organic matter:

- 1030 sulfate reactions at Pine Point, Canada. *Science*, 224(4644), 63–66.
- 1031 Riciputi, L. E. E. R., Macheu, H. G., & Colp, D. R. (1994). An ion microprobe study of
1032 diagenetic carbonates in the devonian nisku formation of Alberta, Canada. *Geochimica et*
1033 *Cosmochimica Acta*, (1), 115–127. Retrieved from
1034 <http://www.sciencedirect.com/science/article/pii/0016703796831334>
- 1035 Roberts, A. E. (1966). Stratigraphy of the Madison Group near Livingston, Montana and
1036 discussion of karst and solution-breccia features. *U. S. Geological Survey Professional*
1037 *Paper*, (526–B), B1–B23. techreport.
- 1038 Roberts, L. N. R., Lewan, M. D., & Finn, T. M. (2005). Burial history, thermal maturity, and oil
1039 and gas generation history of petroleum systems in the southwestern Wyoming province,
1040 Wyoming, Colorado and Utah. *US Geological Survey Southwest Wyoming Province*
1041 *Assessment Team: Petroleum Systems and Geologic Assessment of Oil and Gas in the*
1042 *Southwestern Wyoming Province, Wyoming, Colorado, and Utah: US Geological Survey*
1043 *Digital Data Series DDS-69-D*.
- 1044 Robinson, B. W., & Kusakabe, M. (1975). Quantitative preparation of sulfur dioxide, for sulfur-
1045 34/sulfur-32 analyses, from sulfides by combustion with cuprous oxide. *Analytical*
1046 *Chemistry*, 47(7), 1179–1181.
- 1047 Romanek, C. S., Grossman, E. L., & Morse, J. W. (1992). Carbon isotopic fractionation in
1048 syntetic aragonite and calcite: effects of temperature and precipitation rate. *Geochimica et*
1049 *Cosmochimica Acta*, 56, 419–430. Retrieved from
1050 <http://www.sciencedirect.com/science/article/pii/0016703792901426>
- 1051 Sando, W. J. (1976). Mississippi history of the northern rocky mountains region. *Journal of*
1052 *Research of the U.S. Geological Survey*, 4(3), 317–338.
- 1053 Schmidt, K., Koschinsky, A., Garbe-Schönberg, D., de Carvalho, L. M., & Seifert, R. (2007).
1054 Geochemistry of hydrothermal fluids from the ultramafic-hosted Logatchev hydrothermal
1055 field, 15 N on the Mid-Atlantic Ridge: temporal and spatial investigation. *Chemical*
1056 *Geology*, 242(1), 1–21.
- 1057 Sheppard, S. M. F., & Schwarz, H. P. (1970). Fractionation of carbon and oxygen isotopes and
1058 magnesium between coexisting metamorphic calcite and dolomite. *Contributions to*
1059 *Mineralogy and Petrology*, 26(3), 161–198.
- 1060 Smith, L. B., Eberli, G. P., & Sonnenfeld, M. (2004). Sequence-stratigraphic and
1061 paleogeographic distribution of reservoir-quality dolomite, Madison Formation, Wyoming
1062 and Montana. *Integration of Outcrop and Modern Analogs in Reservoir Modeling, AAPG*
1063 *Memoir 80*, 80, 67–92. [https://doi.org/10.1306/61EED030-173E-11D7-](https://doi.org/10.1306/61EED030-173E-11D7-8645000102C1865D)
1064 [8645000102C1865D](https://doi.org/10.1306/61EED030-173E-11D7-8645000102C1865D)
- 1065 Smith, T. M. (1991). *Diagenesis of shallow marine carbonate rocks: Isotopic and trace element*
1066 *constraints from the Mississippian Mission Canyon Formation, central and southwestern*
1067 *Montana*. Texas A&M University.

- 1068 Sonnenfeld, M. (1996a). *An Integrated Sequence Stratigraphic Approach to Reservoir*
1069 *Characterization of the Lower Mississippian Madison Limestone, Emphasizing Elk Basin*
1070 *Field, Bighorn Basin, Wyoming and Montana*. Colorado School of Mines. Retrieved from
1071 <https://books.google.co.uk/books?id=g4TatwAACAAJ>
- 1072 Sonnenfeld, M. (1996b). Sequence evolution and hierarchy within the lower Mississippian
1073 Madison Limestone of Wyoming. *Paleozoic Systems of the Rocky Mountain Region*, 165–
1074 192. Retrieved from
1075 [http://archives.datapages.com/data/rocky_sepm/data/034/034001/165_rocky_mount340165.](http://archives.datapages.com/data/rocky_sepm/data/034/034001/165_rocky_mount340165.htm)
1076 [htm](http://archives.datapages.com/data/rocky_sepm/data/034/034001/165_rocky_mount340165.htm)
- 1077 Stilwell, D. P. (1989). CO₂ resources of the Moxa Arch and the Madison Reservoir, 105–115.
- 1078 Strebel, O., Böttcher, J., & Fritz, P. (1990). Use of isotope fractionation of sulfate-sulfur and
1079 sulfate-oxygen to assess bacterial desulfurication in a sandy aquifer. *Journal of Hydrology*,
1080 *121*(1–4), 155–172. [https://doi.org/10.1016/0022-1694\(90\)90230-U](https://doi.org/10.1016/0022-1694(90)90230-U)
- 1081 Sverjensky, D. A. (1984). Europium redox equilibria in aqueous solution. *Earth and Planetary*
1082 *Science Letters*, *67*(1), 70–78.
- 1083 Tanaka, K., & Kawabe, I. (2006). REE abundances in ancient seawater inferred from marine
1084 limestone and experimental REE partition coefficients between calcite and aqueous
1085 solution. *Geochemical Journal*, *40*(5), 425–435. <https://doi.org/10.2343/geochemj.40.425>
- 1086 Thayer, P. A. (1983). Relationship of Porosity and Permeability to Petrology of the Madison
1087 Limestone in Rock Cores from Three Test WeUs in Montana and Wyoming Relationship of
1088 Porosity and Permeability to Petrology of the Madison Limestone in Rock Cores from
1089 Three Test Wells i. *Geological Survey Paper 1273-C*. Retrieved from
1090 <https://pubs.er.usgs.gov/pubs/pp/pp1273C>
- 1091 Veizer, J., Godderis, Y., & François, L. M. (2000). Evidence for decoupling of atmospheric CO₂
1092 and global climate during the Phanerozoic eon. *Nature*, *408*(6813), 698–701.
1093 <https://doi.org/10.1038/35047044>
- 1094 Wach, P. H. (1977). The Moxa Arch, an overthrust model? *Wyoming Geological Association*,
1095 *29th Annual Field Conference*, 651–664.
- 1096 Wallmann, K. (2004). Impact of atmospheric CO₂ and galactic cosmic radiation on Phanerozoic
1097 climate change and the marine $\delta^{18}\text{O}$ record. *Geochemistry, Geophysics, Geosystems*, *5*(6).
1098 <https://doi.org/10.1029/2003GC000683>
- 1099 Williams, R. H., & Paulo, S. (2002). Major Roles for Fossil Fuels in an Environmentally
1100 Constrained World. *Sustainability in Energy Production and Utilization in Brazil: The next*
1101 *Twenty Years, 2002*(February), 18–20. Retrieved from
1102 [http://www.feagri.unicamp.br/energia/energia2002/jdownloads/pdf/papers/paper_Williams.](http://www.feagri.unicamp.br/energia/energia2002/jdownloads/pdf/papers/paper_Williams.pdf)
1103 [pdf](http://www.feagri.unicamp.br/energia/energia2002/jdownloads/pdf/papers/paper_Williams.pdf)
- 1104 Worden, R. H., & Smalgeoley, P. C. (1996). H₂S-producing reactions in deep carbonate gas
1105 reservoirs: Khuff Formation, Abu Dhabi. *Chemical Geology*, *133*(1), 157–171.

- 1106 Worden, R. H., Smalley, P. C., & Oxtoby, N. H. (1995). Gas souring by thermochemical sulfate
1107 reduction at 140 C. *AAPG Bulletin*, 79(6), 854–863.
- 1108 Worden, R. H., Smalley, P. C., & Cross, M. M. (2000). The influence of rock fabric and
1109 mineralogy on thermochemical sulfate reduction: Khuff Formation, Abu Dhabi. *Journal of*
1110 *Sedimentary Research*, 70(5).
- 1111 Wynn, J. G., Sumrall, J. B., & Onac, B. P. (2010). Sulfur isotopic composition and the source of
1112 dissolved sulfur species in thermo-mineral springs of the Cerna Valley, Romania. *Chemical*
1113 *Geology*, 271(1–2), 31–43. <https://doi.org/10.1016/j.chemgeo.2009.12.009>
- 1114 Wynn, P. M., Fairchild, I. J., Baker, A., Baldini, J. U. L., & McDermott, F. (2008). Isotopic
1115 archives of sulphate in speleothems. *Geochimica et Cosmochimica Acta*, 72(10), 2465–
1116 2477.
- 1117 Wynn, P. M., Loader, N. J., & Fairchild, I. J. (2014). Interrogating trees for isotopic archives of
1118 atmospheric sulphur deposition and comparison to speleothem records. *Environmental*
1119 *Pollution*, 187, 98–105. <https://doi.org/http://dx.doi.org/10.1016/j.envpol.2013.12.017>
- 1120 Xiao, Y., Xu, T., & Pruess, K. (2009). The effects of gas-fluid-rock interactions on CO₂
1121 injection and storage: Insights from reactive transport modeling. *Energy Procedia*, 1(1),
1122 1783–1790. <https://doi.org/http://dx.doi.org/10.1016/j.egypro.2009.01.233>
- 1123 Yue, C., Li, S., Ding, K., & Zhong, N. (2005). Study of simulation experiments on the TSR
1124 system and its effect on the natural gas destruction. *Science in China Series D: Earth*
1125 *Sciences*, 48(8), 1197–1202. <https://doi.org/10.1360/03yd0133>
- 1126 Yue, C., Li, S., Ding, K., & Zhong, N. (2006). Thermodynamics and kinetics of reactions
1127 between C₁–C₃ hydrocarbons and calcium sulfate in deep carbonate reservoirs.
1128 *Geochemical Journal*, 40(1), 87–94.
- 1129 Zhang, W., Xu, T., & Li, Y. (2011). Modeling of fate and transport of coinjection of H₂S with
1130 CO₂ in deep saline formations. *Journal of Geophysical Research: Solid Earth*, 116(B2).
- 1131 Zhong, S., & Mucci, A. (1995). Partitioning of rare earth elements (REEs) between calcite and
1132 seawater solutions at 25 C and 1 atm, and high dissolved REE concentrations. *Geochimica*
1133 *et Cosmochimica Acta*, 59(3), 443–453.

1134

1135

1136 Figure captions

1137

1138 **Figure 1a)** Map of the Moxa Arch with main tectonic features in the area modified after Becker and Lynds, (2012).
1139 The LaBarge Field is coloured in grey. b) Map of the LaBarge Field with contour lines of the top of the Madison
1140 Formation and gas water contact in TVD SS modified after (Stilwell, 1989) c) integrity of three viewed drill cores
1141 and their relative depth in the Moxa Arch.

1142

1143 **Figure 2** Burial history modified after Roberts et al., (2005) and adapted to 500 m further uplift at the LaBarge Field
1144 in the last 5 Ma. The Madison Formation is highlighted in grey. Fm., Formation; Sh., Shale; Gp., Group; Ss.,
1145 Sandstone; L. Cret., Lower Cretaceous rocks. The surface temperature has been set at 25°C.

1146

1147 **Figure 3** a & b) Madison limestone consisting of partially micritized foraminifers, brachiopods, bivalve and
 1148 echinoderm fragments with micro-spar filling the pore space c) fabric preserving euhedral to subhedral dolomite
 1149 with high intercrystalline porosity, d) fabric preserving euhedral to subhedral dolomite with poikilotopic calcite
 1150 cement filling the pore space, e) partially silicified dolomite breccia f) fracture-filling calcite in dolomite host rock
 1151 (sample C6), g) former anhydrite nodule replaced by calcite with elemental sulphur precipitated in between calcite
 1152 crystals (sample S2), h) former anhydrite nodule replaced by a succession of chalcedony and quartz precipitated in
 1153 the rim, followed by 100-500 μm sized calcite crystals (sample A1(F)) and a cm sized calcite crystal in the centre
 1154 (sample A1(C)).

1155

1156 **Figure 4** a-c) Rare earth element patterns from fracture-filling calcite, calcite that replaced anhydrite, 3 dissimilar
 1157 calcite that replaced anhydrite samples and seawater (Mitra et al., 1994). d) Barium and Europium concentrations.
 1158 Squares are fracture-filling calcite samples whereas circles are calcite that replaced anhydrite samples and triangles
 1159 are the 3 dissimilar calcite that replaced anhydrite samples. The samples from plot (b) correlate in their Ba and Eu
 1160 concentration and hence a severe BaO interference can't be ruled out. The fracture-filling calcite samples (a) and the
 1161 three samples from plot (c) lie above the correlation trend and have a reliable Eu concentration. e) Cerium anomaly
 1162 diagram from Bau and Dulski, (1996). Samples in the bottom right quadrant have true cerium anomalies. The calcite
 1163 that replaced anhydrite sample with two different calcite textures was analyzed in the core and rim of the nodule and
 1164 is marked with a black line between the two measurement points. Black, grey and white symbols represent samples
 1165 from drill core FC13-10, LR8-11 and FC15-28 respectively.

1166

1167 **Figure 5** Carbon and oxygen isotopic data from carbonate samples. Sample A1 is marked with a black dotted line
 1168 between the core (A1(C)) and the rim (A1(F)) measurement. Black, grey, white and crossed symbols represent
 1169 samples from drill core FC13-10, LR8-11, FC15-28 and LR4-22 respectively.

1170

1171 **Figure 6** a) Sulphur isotopes in pyrite (diamonds) and native sulphur (triangles). b) CAS oxygen and sulphur
 1172 isotopes in fracture-filling calcite (square) and nodular calcite that replaced anhydrite (circles). There is a strong
 1173 correlation between the two isotopic values. c & d) CAS oxygen and sulphur isotopes versus carbon isotopes in
 1174 calcites that replace anhydrite. Sample A1 is marked with a black line between the core (A1(C)) and the rim (A1(F))
 1175 measurement where the core of the sample with a cm sized calcite crystal is marked with a double circle. This
 1176 double circled sample lies between the two trends indicated by the arrows. Black, grey and white symbols represent
 1177 samples from drill core FC13-10, LR8-11 and FC15-28 respectively.

1178

1179 **Figure 7** Fluid inclusion homogenisation temperatures of primary (p) and secondary (s) fluid inclusion assemblages
 1180 (FIA) in microspar, quartz, fracture-filling calcite, fluorite, saddle dolomite and calcite that replaced anhydrite.
 1181 Samples from drill core FC13-10, FC15-28 and LR8-11 have black, white and grey filling colours, respectively. FIA
 1182 measured in the same sample are bracketed and in one quartz crystal a transect from core to rim has been measured.

1183

1184 **Figure 8** Precipitated mineral phases and fluid inputs with increasing time.

1185

1186 **Table 1** Rare earth element and yttrium concentrations and their relative standard error.

1187

1188 **Table 2** Stable isotope data from fracture-filling calcite (FFC), calcite that replaced anhydrite (CRA), saddle
 1189 dolomite (SD), pyrite (Py), elemental sulphur (S) and quartz (Q).

1190

1191 **Table 3** Homogenisation temperatures, freezing point depressions, and calculated salinities from fluid inclusion
 1192 assemblages in quartz, fluorite and calcite. Each row represents a distinct fluid inclusion assemblage according to
 1193 the criteria of Goldstein and Reynolds (1994).

1194

Appendix 1 Sample C14 (left) and A1 (right): calcite that replaced anhydrite with anhydrite micro inclusions.

Figure 1.

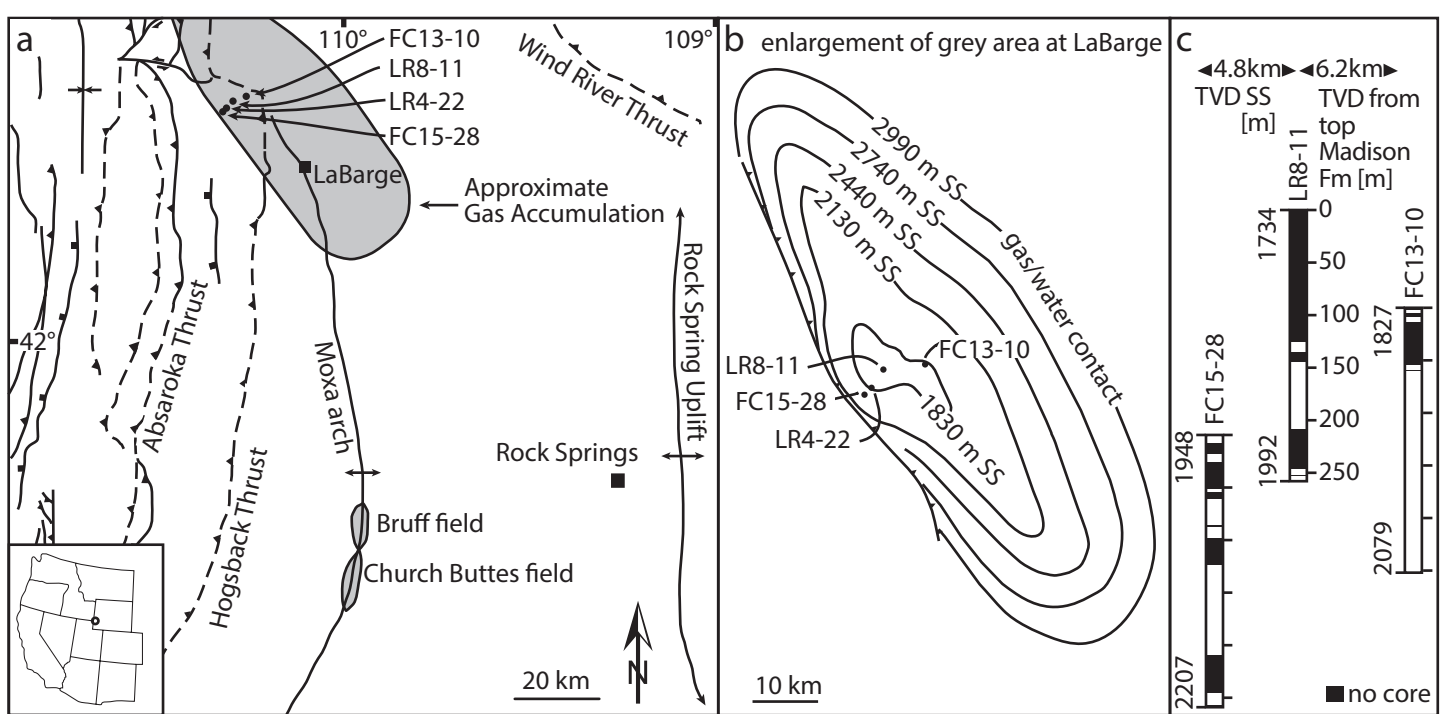


Figure 2.

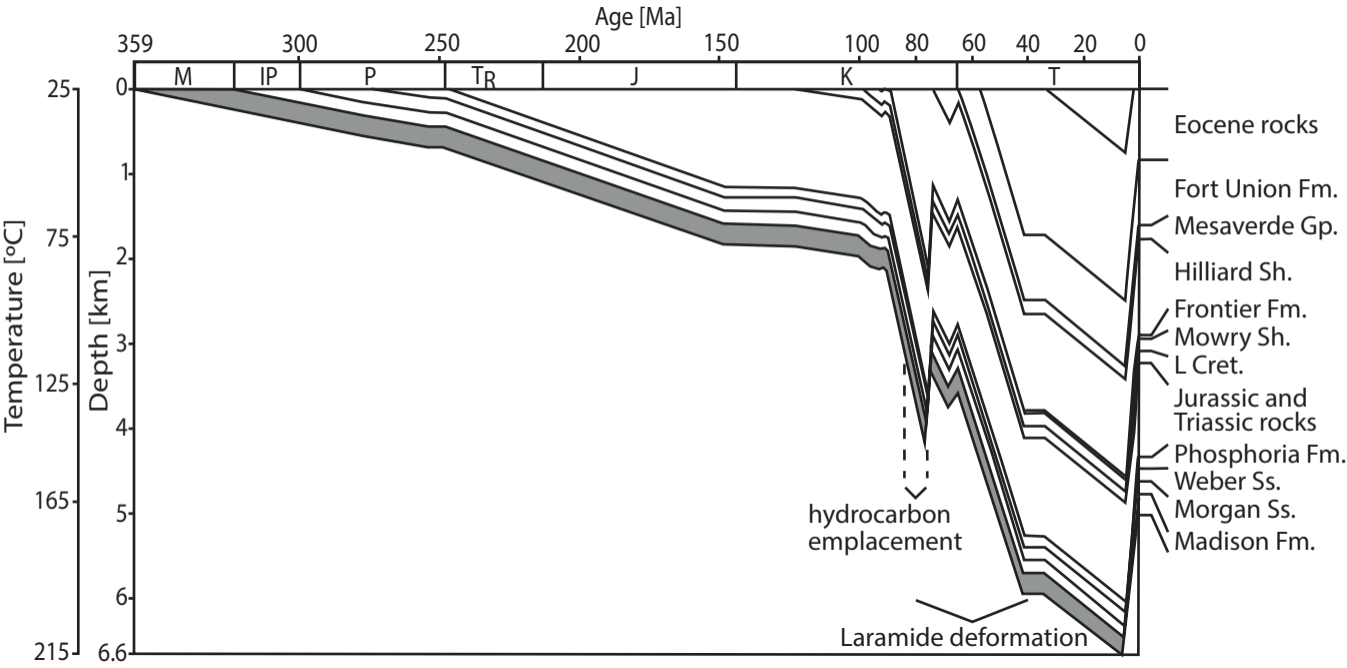


Figure 3.

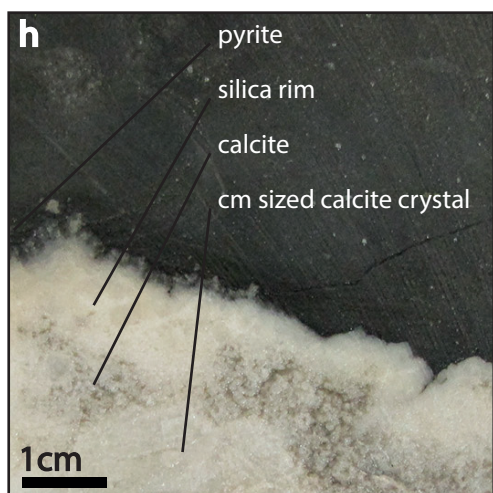
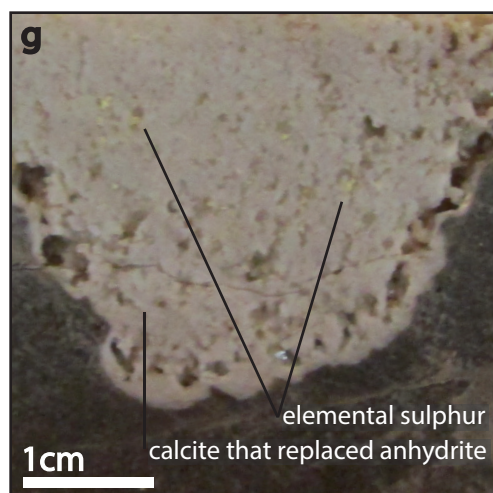
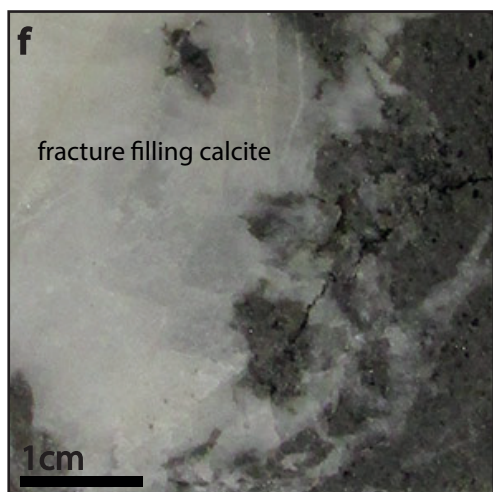
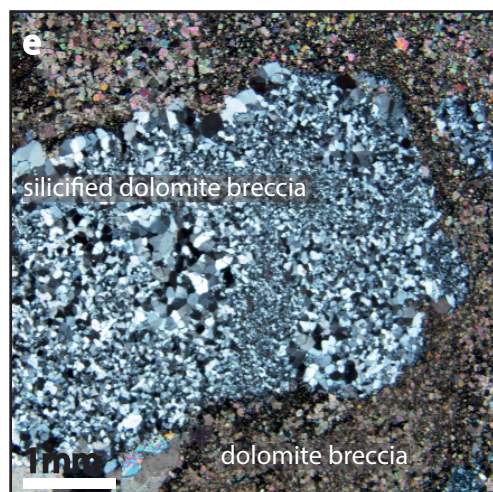
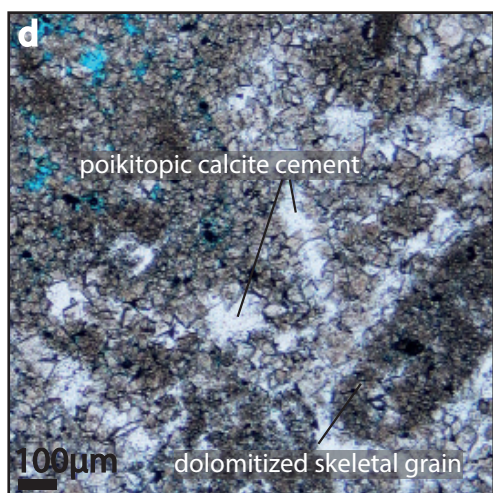
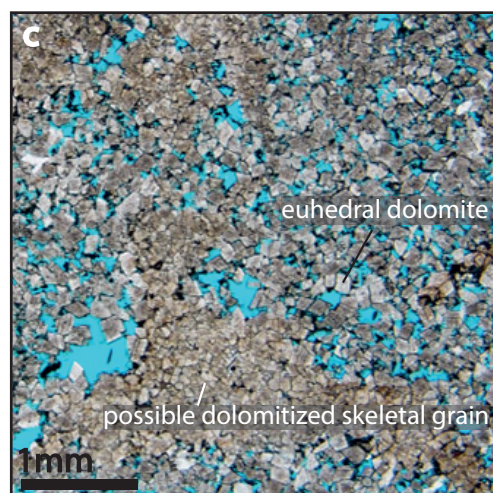
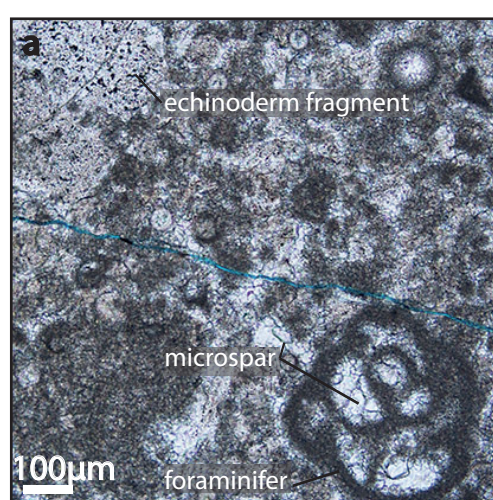


Figure 4.

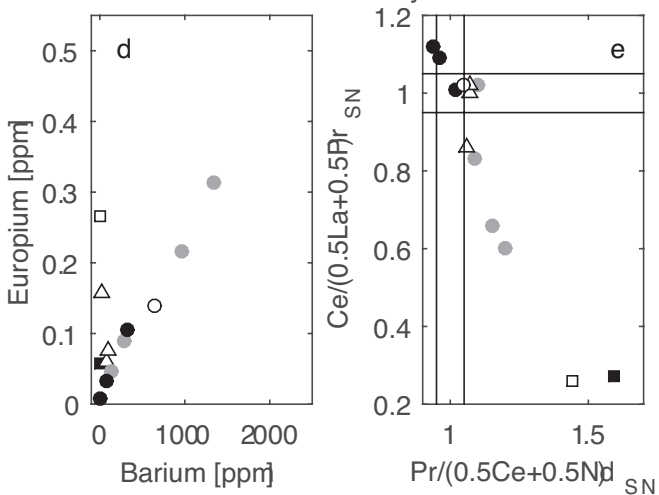
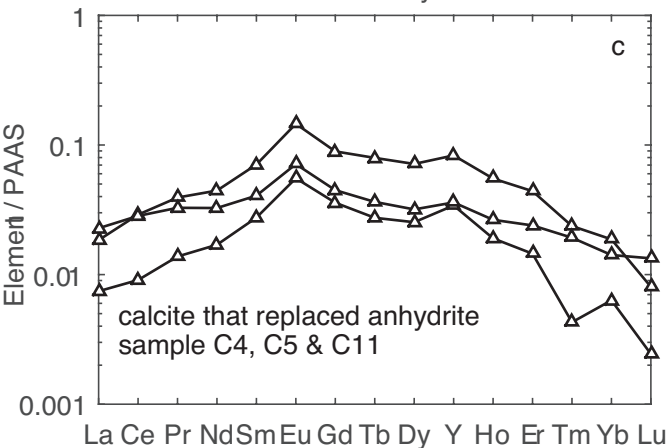
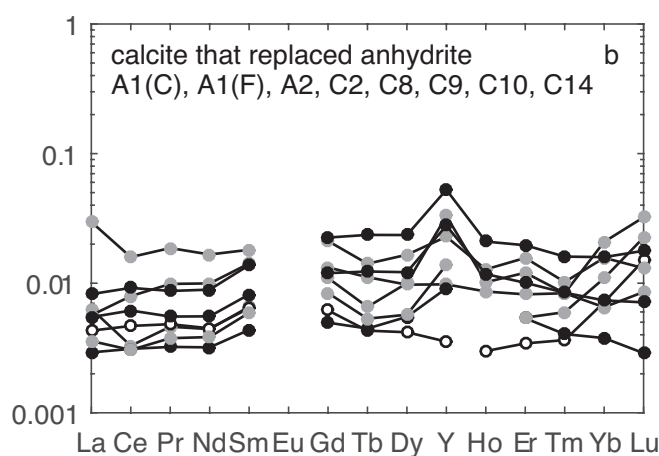
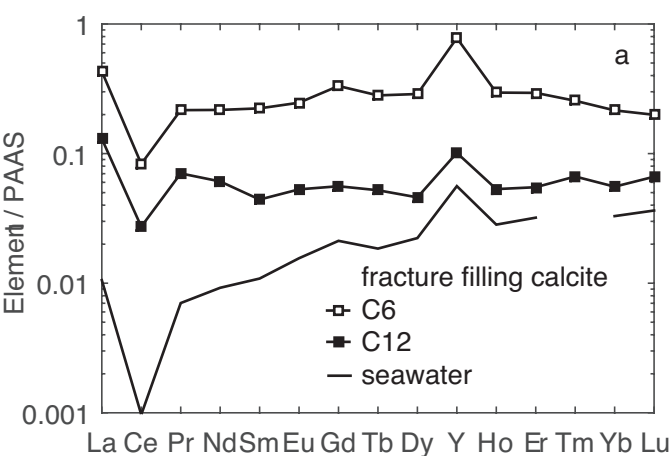


Figure 5.

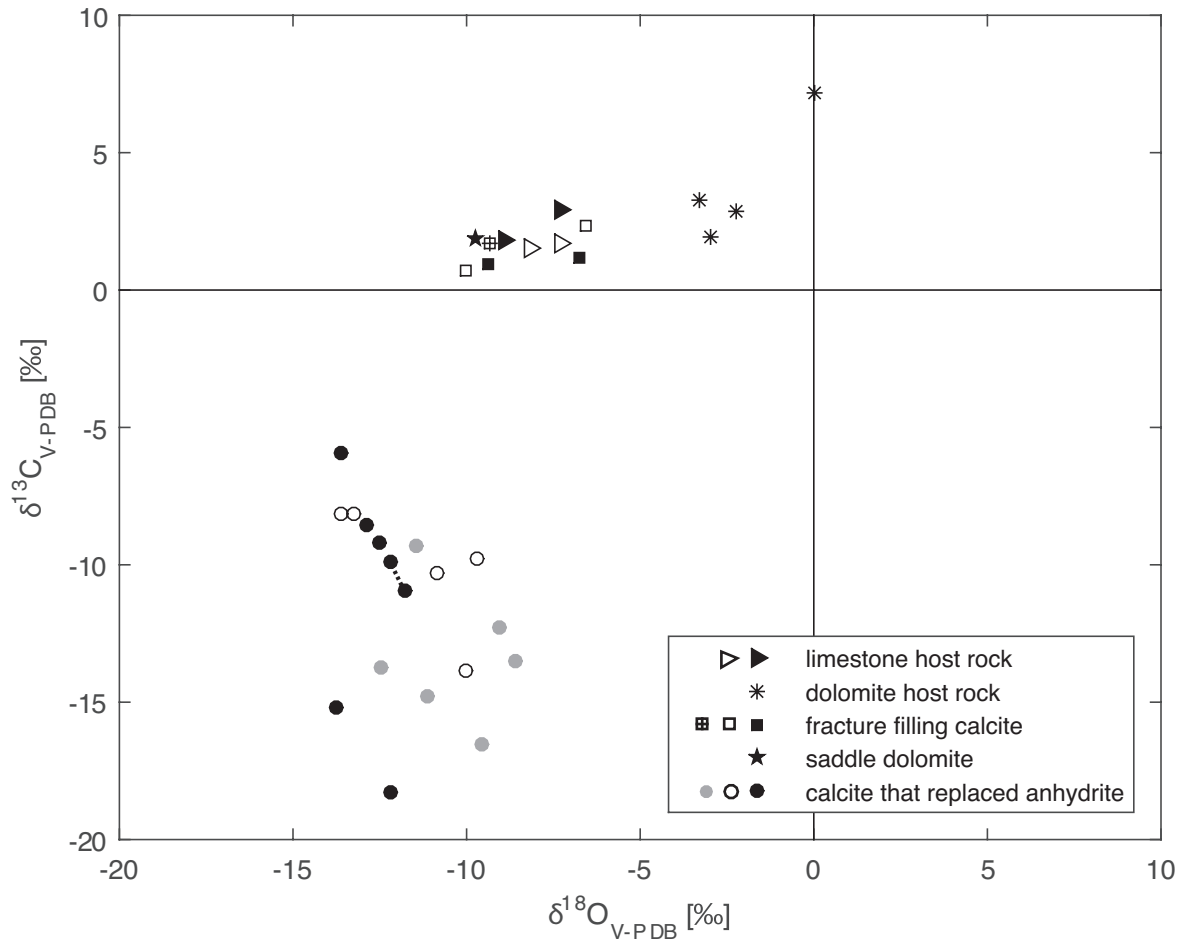


Figure 6.

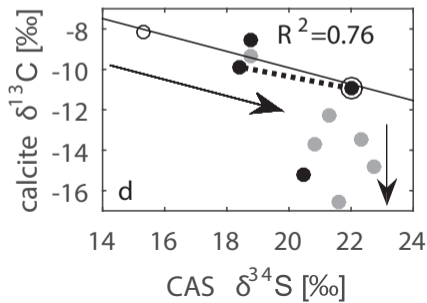
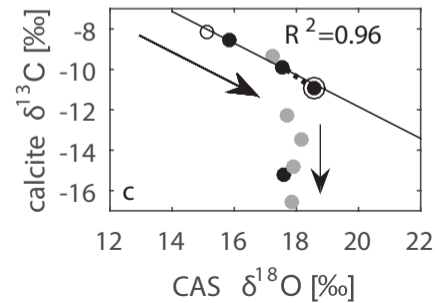
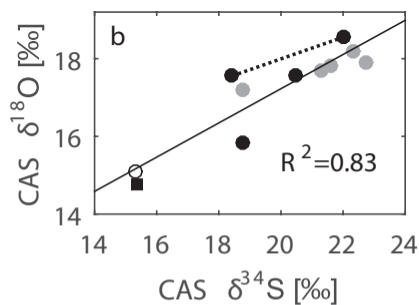
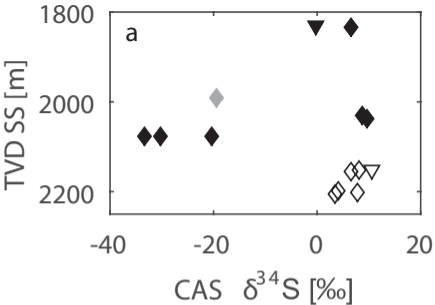


Figure 7.

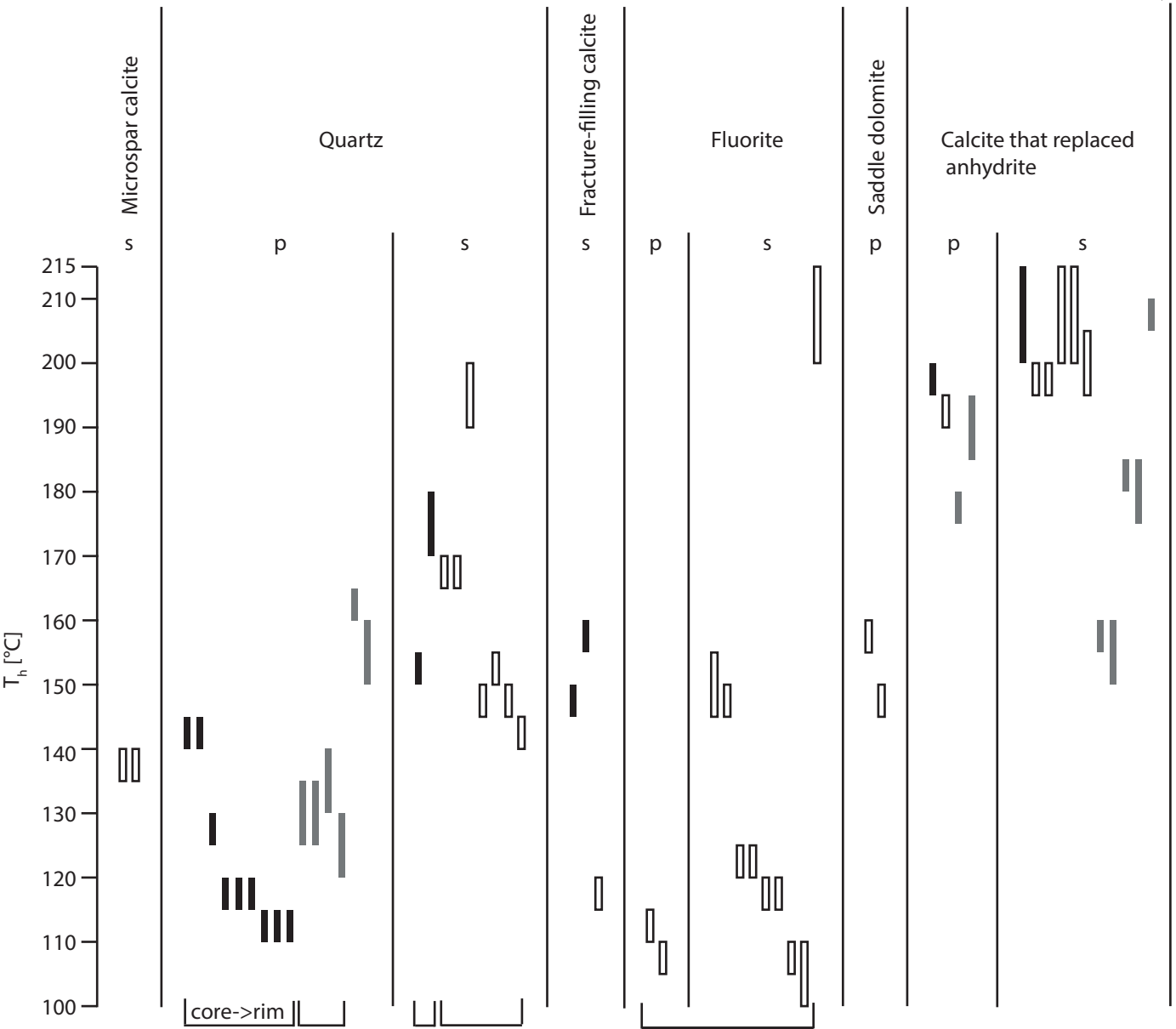
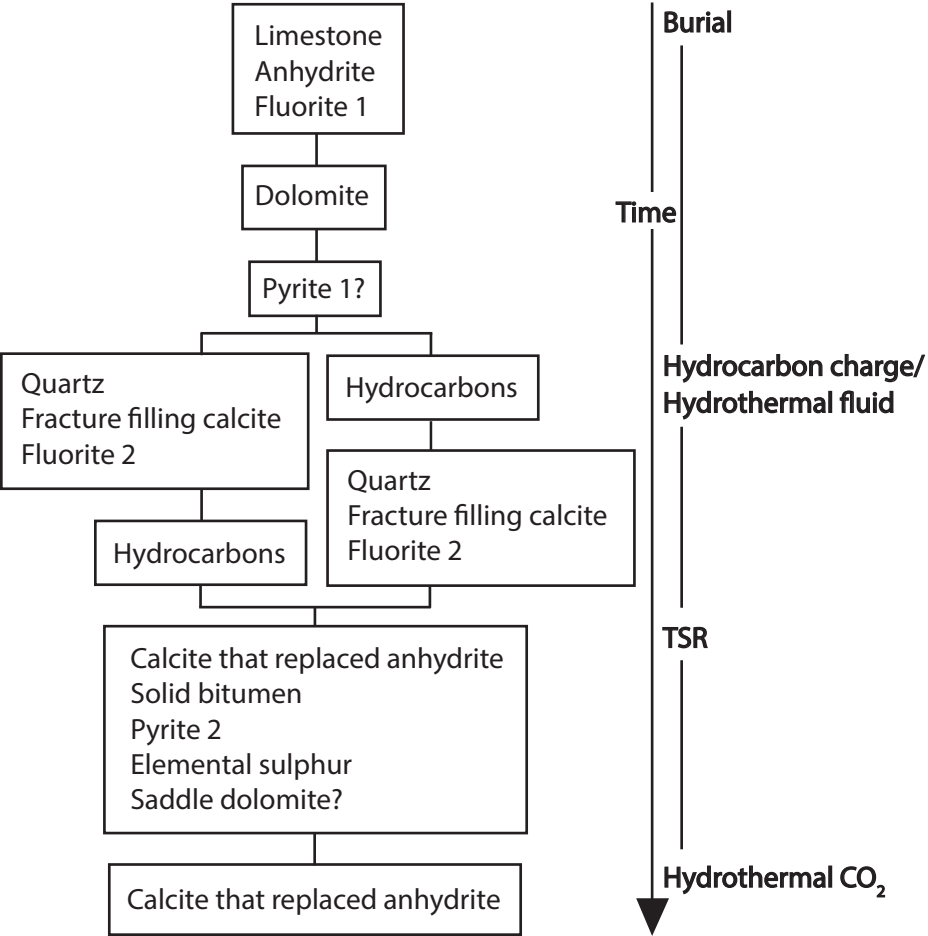
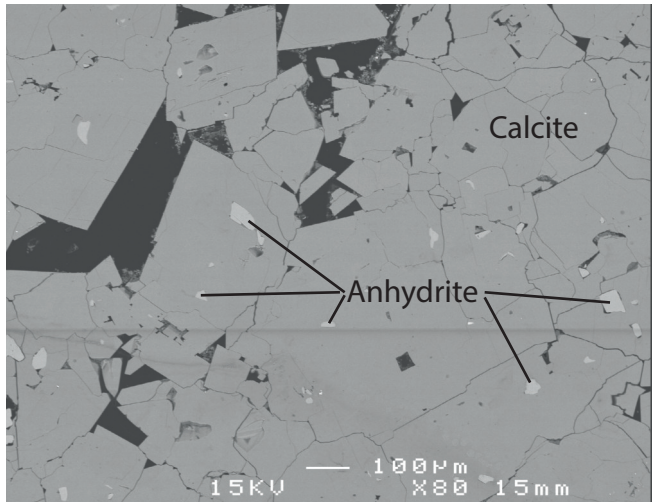
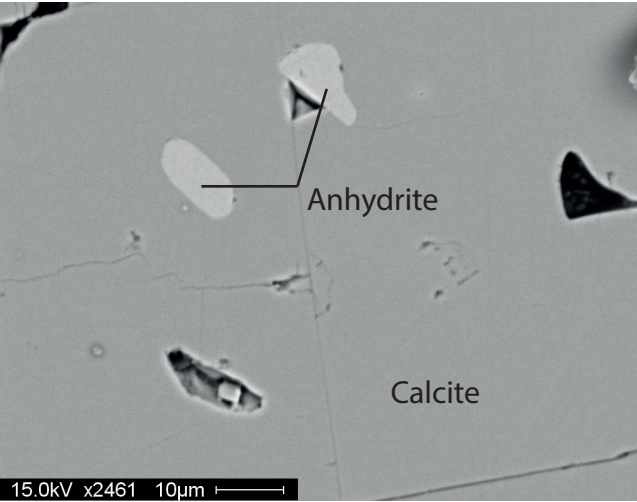


Figure 8.



Appendix 1.



| Drill core | Sample ID | Mineral phase | Distance to top Madison [m] | TVD SS [m] | Carbonate $\delta^{13}\text{C}_{\text{V-PDB}}$ [‰] | Carbonate $\delta^{18}\text{O}_{\text{V-PDB}}$ [‰] | Pyrite/Sulphur $\delta^{34}\text{S}_{\text{V-CDT}}$ [‰] | CAS $\delta^{34}\text{S}_{\text{V-CDT}}$ [‰] | CAS $\delta^{18}\text{O}_{\text{V-SMOW}}$ [‰] | Quartz $\delta^{18}\text{O}_{\text{V-SMOW}}$ [‰] | REE measurement |
|------------|-----------|---|-----------------------------|------------|--|--|---|--|---|--|-----------------|
| FC13-10 | S1 | Elemental Sulphur | 3.4 | 1830.4 | | | -0.2 | | | | |
| FC13-10 | P4 | Pyrite | 249.6 | 2076.6 | | | -30.2 | | | | |
| FC13-10 | P5(1) | Pyrite | 250.3 | 2077.3 | | | -33.2 | | | | |
| FC13-10 | P5(2) | Pyrite | 250.3 | 2077.3 | | | -20.5 | | | | |
| FC13-10 | P1 | Pyrite | 8.4 | 1835.4 | | | 6.6 | | | | |
| FC13-10 | P2 | Pyrite | 203.9 | 2030.9 | | | 8.8 | | | | |
| FC13-10 | P3 | Pyrite | 210.5 | 2037.5 | | | 9.5 | | | | |
| FC13-10 | A1(C) | Calcite that replaced Anhydrite (core) | 245.8 | 2072.8 | -11.0 | -11.8 | | 22.0 | 18.6 | | yes |
| FC13-10 | A1(F) | Calcite that replaced Anhydrite (rim) | 245.8 | 2072.8 | -9.9 | -12.2 | | 18.4 | 17.6 | | yes |
| FC13-10 | A2 | Calcite that replaced Anhydrite | 253.6 | 2080.6 | -8.6 | -12.9 | | 18.8 | 15.9 | | yes |
| FC13-10 | C12 | Fracture-filling Calcite | 107.3 | 1934.3 | 1.2 | -6.8 | | 15.3 | 14.7 | | yes |
| FC13-10 | C13 | Calcite that replaced Anhydrite | 176.1 | 2003.1 | -15.2 | -13.7 | | 20.5 | 17.6 | | |
| FC13-10 | C7 | Calcite that replaced Anhydrite | 241.4 | 2068.4 | -9.2 | -12.5 | | x | x | | |
| FC13-10 | C7(L) | Limestone | 241.4 | 2068.4 | 1.8 | -8.9 | | | | | |
| FC13-10 | A3 | Calcite that replaced Anhydrite | 242.2 | 2069.2 | -5.9 | -13.6 | | x | x | | x |
| FC13-10 | D1 | Dolomite | 169.8 | 1996.8 | 3.3 | -3.3 | | | | | |
| FC13-10 | D2 | Dolomite | 82.0 | 1909.0 | 1.9 | -2.9 | | | | | |
| FC13-10 | D3 | Dolomite | 147.3 | 1974.3 | 2.9 | -2.2 | | | | | |
| FC13-10 | D4 | Dolomite | 213.3 | 2040.3 | 7.2 | 0.0 | | | | | |
| FC13-10 | L1(1) | Limestone | 157.6 | 1984.6 | 1.5 | -8.2 | | | | | |
| FC13-10 | L1(2) | Limestone | 157.6 | 1984.6 | 1.7 | -7.3 | | | | | |
| FC13-10 | A4(D) | Saddle Dolomite | 230.6 | 2057.6 | 1.9 | -9.8 | | | | | |
| FC13-10 | A4 | Fracture-filling Calcite | 230.6 | 2057.6 | 1.0 | -9.4 | | | | | |
| FC13-10 | A4(L) | Limestone | 230.6 | 2057.6 | 2.9 | -7.3 | | | | | |
| FC13-10 | Q1 | Quartz | 175.0 | 2002.0 | | | | | | 27.5 | |
| FC13-10 | Q2 | Calcite that replaced Anhydrite and Quartz | 12.6 | 1839.6 | -18.3 | -12.2 | | | | 28.1 | |
| FC15-28 | S2 | Calcite that replaced Anhydrite/Elemental Sulphur | 205.2 | 2153.2 | -8.2 | -13.3 | 10.7 | | | | |
| FC15-28 | P6 | Pyrite | 205.7 | 2153.7 | | | 8.0 | | | | |
| FC15-28 | P7 | Pyrite | 209.0 | 2157.0 | | | 6.6 | | | | |
| FC15-28 | P8 | Pyrite | 249.4 | 2197.4 | | | 4.1 | | | | |
| FC15-28 | P9 | Pyrite | 255.0 | 2203.0 | | | 7.9 | | | | |
| FC15-28 | P10 | Pyrite | 257.0 | 2205.0 | | | 3.6 | | | | |
| FC15-28 | C10 | Calcite that replaced Anhydrite | 62.3 | 2010.3 | -8.2 | -13.6 | | 15.3 | 15.1 | | yes |
| FC15-28 | C5 | Calcite that replaced Anhydrite | 255.0 | 2203.0 | -13.9 | -10.0 | | x | x | | yes |
| FC15-28 | C4 | Calcite that replaced Anhydrite | 255.1 | 2203.1 | -9.8 | -9.7 | | x | x | | yes |
| FC15-28 | C11 | Calcite that replaced Anhydrite | 206.3 | 2154.3 | -10.3 | -10.9 | | x | x | | yes |
| FC15-28 | A5 | Fracture-filling Calcite | 172.8 | 2120.8 | 2.3 | -6.6 | | | | | |
| FC15-28 | C6 | Fracture-filling Calcite | 135.3 | 2083.3 | 0.7 | -10.0 | | | | | yes |
| LR4-22 | LB2 | Fracture-filling Calcite | 136.9 | 1920.0 | 1.7 | -9.3 | | | | | |
| LR8-11 | P11 | Pyrite | 256.9 | 1990.9 | | | -19.5 | | | | |
| LR8-11 | C1 | Calcite that replaced Anhydrite | 254.8 | 1988.8 | -16.6 | -9.6 | | 21.6 | 17.8 | | x |
| LR8-11 | C14 | Calcite that replaced Anhydrite | 249.3 | 1983.3 | -12.3 | -9.1 | | 21.3 | 17.7 | | yes |
| LR8-11 | C2 | Calcite that replaced Anhydrite | 206.3 | 1940.3 | -14.8 | -11.1 | | 22.7 | 17.9 | | yes |
| LR8-11 | C3 | Calcite that replaced Anhydrite and Quartz | 251.0 | 1985.0 | -13.5 | -8.6 | | 22.3 | 18.2 | 28.1 | |
| LR8-11 | C8 | Calcite that replaced Anhydrite | 172.9 | 1906.9 | -9.3 | -11.4 | | 18.8 | 17.2 | | yes |
| LR8-11 | C9 | Calcite that replaced Anhydrite | 152.8 | 1886.8 | -13.7 | -12.5 | | 20.9 | x | | yes |

| Drill core | Sample | 137 Ba | | 139 La | | 140 Ce | | 141 Pr | | 146 Nd | | 147 Sm | |
|------------|--------|---------|-----|--------|-----|--------|-----|--------|-----|--------|-----|--------|-------|
| | ID | [ppm] | RSD | [ppm] | RSD | [ppm] | RSD | [ppm] | RSD | [ppm] | RSD | [ppm] | RSD |
| FC15-28 | C6 | 6.07 | 1.2 | 16.47 | 0.5 | 6.63 | 2.4 | 1.91 | 0.4 | 7.37 | 0.5 | 1.24 | 1.97 |
| FC13-10 | C12 | 2.12 | 1.5 | 4.97 | 0.6 | 2.17 | 1.2 | 0.62 | 0.8 | 2.07 | 1.0 | 0.25 | 1.45 |
| FC15-28 | C5 | 76.62 | 0.5 | 0.28 | 1.7 | 0.72 | 0.9 | 0.12 | 1.1 | 0.58 | 0.4 | 0.15 | 3.84 |
| FC15-28 | C4 | 15.19 | 0.1 | 0.70 | 1.4 | 2.31 | 0.1 | 0.35 | 0.5 | 1.51 | 1.3 | 0.39 | 1.36 |
| FC15-28 | C11 | 94.91 | 0.2 | 0.87 | 0.7 | 2.26 | 1.1 | 0.29 | 1.3 | 1.11 | 1.3 | 0.23 | 4.08 |
| LR8-11 | C9 | 1346.50 | 1.1 | 0.24 | 1.9 | 0.26 | 1.7 | 0.04 | 3.6 | 0.15 | 1.7 | 0.04 | 2.79 |
| LR8-11 | C8 | 286.51 | 1.0 | 1.13 | 0.8 | 1.27 | 0.8 | 0.16 | 0.6 | 0.56 | 1.8 | 0.10 | 1.70 |
| LR8-11 | C2 | 139.01 | 1.2 | 0.22 | 0.7 | 0.63 | 1.3 | 0.09 | 2.7 | 0.34 | 2.3 | 0.08 | 1.36 |
| FC13-10 | A1(C) | 72.60 | 1.9 | 0.21 | 1.1 | 0.49 | 0.5 | 0.05 | 2.2 | 0.19 | 2.7 | 0.05 | 8.79 |
| FC13-10 | A2 | 5.61 | 2.1 | 0.11 | 2.9 | 0.25 | 1.8 | 0.03 | 3.5 | 0.11 | 1.5 | 0.02 | 4.75 |
| LR8-11 | C14 | 961.26 | 1.0 | 0.14 | 1.5 | 0.24 | 0.4 | 0.03 | 2.5 | 0.13 | 4.2 | 0.03 | 5.51 |
| FC13-10 | A1(F) | 320.22 | 1.3 | 0.31 | 1.1 | 0.73 | 0.5 | 0.08 | 2.3 | 0.30 | 2.0 | 0.08 | 2.88 |
| FC15-28 | C10 | 638.70 | 0.8 | 0.16 | 2.4 | 0.37 | 3.1 | 0.04 | 1.1 | 0.15 | 4.1 | 0.04 | 12.95 |

| | | 159 Tb | | 163 Dy | | 89 Y | | 165 Ho | | 166 Er | | 169 Tm | |
|------------|--------|--------|------|--------|-----|-------|-----|--------|-----|--------|-----|--------|------|
| drill core | Sample | [ppm] | RSD | [ppm] | RSD | [ppm] | RSD | [ppm] | RSD | [ppm] | RSD | [ppm] | RSD |
| FC15-28 | C6 | 0.218 | 1.2 | 1.349 | 0.7 | 21.04 | 1.5 | 0.293 | 1.3 | 0.838 | 0.7 | 0.104 | 0.9 |
| FC13-10 | C12 | 0.040 | 3.4 | 0.215 | 1.7 | 2.73 | 0.6 | 0.053 | 3.1 | 0.157 | 1.2 | 0.027 | 3.5 |
| FC15-28 | C5 | 0.021 | 4.0 | 0.119 | 2.5 | 0.92 | 0.2 | 0.019 | 2.9 | 0.041 | 4.3 | 0.002 | 10.8 |
| FC15-28 | C4 | 0.062 | 1.2 | 0.334 | 1.3 | 2.24 | 0.4 | 0.055 | 0.8 | 0.126 | 1.6 | 0.010 | 6.4 |
| FC15-28 | C11 | 0.028 | 1.3 | 0.149 | 1.0 | 0.97 | 0.3 | 0.026 | 1.6 | 0.068 | 4.2 | 0.008 | 3.7 |
| LR8-11 | C9 | 0.005 | 3.3 | 0.047 | 5.7 | 0.89 | 0.6 | 0.010 | 6.0 | 0.034 | 2.5 | 0.003 | 3.4 |
| LR8-11 | C8 | 0.011 | 3.7 | 0.078 | 3.8 | 0.62 | 0.7 | 0.013 | 5.4 | 0.045 | 4.1 | 0.004 | 6.4 |
| LR8-11 | C2 | 0.009 | 4.1 | 0.046 | 3.5 | 0.26 | 0.5 | 0.009 | 4.5 | 0.023 | 4.7 | 0.003 | 6.3 |
| FC13-10 | A1(C) | 0.010 | 5.8 | 0.057 | 2.2 | 0.75 | 1.4 | 0.012 | 2.7 | 0.029 | 3.6 | 0.003 | 4.9 |
| FC13-10 | A2 | 0.003 | 13.9 | 0.026 | 5.3 | 0.25 | 1.5 | x | x | 0.015 | 0.9 | 0.002 | 5.9 |
| LR8-11 | C14 | 0.004 | 4.2 | 0.027 | 6.5 | 0.37 | 1.7 | x | x | 0.015 | 4.5 | 0.002 | 7.9 |
| FC13-10 | A1(F) | 0.018 | 2.1 | 0.110 | 0.6 | 1.42 | 1.0 | 0.021 | 3.6 | 0.056 | 3.1 | 0.006 | 3.9 |
| FC15-28 | C10 | 0.003 | 9.0 | 0.020 | 7.7 | 0.10 | 2.4 | x | x | 0.010 | 7.6 | 0.001 | 5.9 |

| 153 Eu | | 157 Gd | |
|---------|-----|---------|------|
| [ppm] | RSD | [ppm] | RSD |
| 0.27 | 0.9 | 1.55 | 1.4 |
| 0.06 | 2.3 | 0.26 | 1.8 |
| 0.06 | 2.3 | 0.17 | 1.9 |
| 0.16 | 2.6 | 0.42 | 1.0 |
| 0.08 | 2.6 | 0.21 | 1.7 |
| x | x | 0.05 | 3.2 |
| x | x | 0.10 | 4.8 |
| x | x | 0.06 | 4.5 |
| x | x | 0.06 | 5.6 |
| x | x | 0.02 | 2.2 |
| x | x | 0.04 | 10.0 |
| x | x | 0.10 | 3.3 |
| x | x | 0.03 | 9.6 |

| 172 Yb | | 175 Lu | |
|---------|------|---------|------|
| [ppm] | RSD | [ppm] | RSD |
| 0.608 | 1.0 | 0.086 | 0.8 |
| 0.157 | 2.9 | 0.029 | 2.2 |
| 0.018 | 4.9 | 0.001 | 13.4 |
| 0.053 | 3.0 | 0.003 | 4.1 |
| 0.040 | 4.6 | 0.006 | 3.6 |
| 0.059 | 4.2 | 0.014 | 3.9 |
| 0.044 | 1.0 | 0.006 | 4.2 |
| 0.018 | 12.3 | 0.004 | 5.2 |
| 0.021 | 5.9 | 0.003 | 14.6 |
| 0.011 | 6.4 | 0.001 | 15.3 |
| 0.031 | 3.3 | 0.010 | 3.3 |
| 0.045 | 2.4 | 0.008 | 6.6 |
| 0.020 | 4.7 | 0.006 | 7.5 |

| Well | TVD SS [m] | T _h (# Fls) [°C] | T _m ice [°C] | NaCl Equivalent Salinity [Wt.%] | Mineral | Comments |
|---------------|------------|-----------------------------|---------------------------------|--|---------------------------------|---|
| FC13-10 | 1839 | 140-145(2) | <-15 | >18.6 | quartz that replaced anhydrite | primaries |
| | | 140-145(2) | <-15 | >18.6 | quartz that replaced anhydrite | primaries |
| | | 125-130(3) | | | quartz that replaced anhydrite | primaries |
| | | 115-120(3) | | | quartz that replaced anhydrite | primaries |
| | | 115-120(2) | -16 | 19.4 | quartz that replaced anhydrite | primaries |
| | | 115-120(2) | -15 | 18.6 | quartz that replaced anhydrite | primaries |
| | | 110-115(5) | <-18 | >21 | quartz that replaced anhydrite | primaries |
| | | 110-115(3) | <-18 | >21 | quartz that replaced anhydrite | primaries |
| | | 110-115(>10) | | | quartz that replaced anhydrite | primaries |
| | | 150-155(4) | >-6 | >9.2 | quartz that replaced anhydrite | secondaries, later gas-rich inclusions |
| 170-180(3) | >-6 | >9.2 | quartz that replaced anhydrite | secondaries, later gas-rich inclusions | | |
| 195-200(>10) | -4.2 | 6.7 | calcite that replaced anhydrite | primaries, Th max | | |
| FC13-10 | 1914 | 145-150 | <-16 | >19.4 | fracture-filling calcite | secondaries, Th max |
| FC13-10 | 2044 | 155-160 | <-16 | >19.4 | fracture-filling calcite | secondaries, Th max |
| FC13-10 | 2072 | 210-215 | >-6 | <9.2 | calcite that replaced anhydrite | secondaries double bubbles clear, Th max |
| FC15-28 | 1952 | 195-200 | >-6 | <9.2 | calcite that replaced anhydrite | secondaries, Th max |
| FC15-28 | 1999 | 115-120 | <-16 | >19.4 | fracture-filling calcite | secondaries, Th max |
| FC15-28 | 2010 | 195-200 | >-6 | <9.2 | calcite that replaced anhydrite | secondaries, Th max |
| FC15-28 | 2020 | 135-140 | <-18 | >21 | microspar calcite cement | secondaries, Th max |
| FC15-28 | 2033 | 135-140 | <-18 | >21 | microspar calcite cement | secondaries, Th max |
| FC15-28 | 2087 | 200-215 | >-6 | <9.2 | calcite that replaced anhydrite | secondaries, Th max |
| FC15-28 | | 155-160 | <-18 | >21 | saddle dolomite | primaries, Th max |
| FC15-28 | 2120 | 190-195 | >-7 | <10.5 | calcite that replaced anhydrite | primaries, Th max |
| | | 110-115(4) | <-18 | >21 | fluorite | primaries |
| | | 105-110(4) | <-18 | >21 | fluorite | primaries in last growth zone |
| | | 150-160(5) | <-18 | >21 | fluorite | secondaries |
| | | 145-150(5) | <-18 | >21 | fluorite | secondaries |
| | | 120-125(4) | <-18 | >21 | fluorite | secondaries |
| | | 120-125(3) | <-18 | >21 | fluorite | secondaries |
| | | 115-120(>10) | <-18 | >21 | fluorite | secondaries |
| | | 115-120(>10) | <-18 | >21 | fluorite | secondaries |
| | | 105-110(6) | <-18 | >21 | fluorite | secondaries |
| 100-110(>100) | -18.6 | 21.4 | fluorite | secondaries | | |
| Well | TVD SS [m] | T _h (# Fls) [°C] | T _m ice [°C] | NaCl Equivalent Salinity [Wt.%] | Mineral | Comments |
| FC15-28 | 2125 | 145-150(>10) | -6.7 | 10 | saddle dolomite | primaries with gas inclusions |
| FC15-28 | 2150 | 200-215 | >-7 | <10.5 | fluorite | secondaries, lots of gas-filled inclusions |
| FC15-28 | 2201 | 200-215 | -12 | 16 | calcite that replaced anhydrite | secondaries, Th max |
| FC15-28 | 2203 | 165-175(5) | -9.2 | 13.1 | quartz | secondaries |
| | | 165-175(4) | -12 | 16 | quartz | secondaries |
| | | 190-200(>10) | | | quartz | secondaries |
| | | 145-150(4) | -5.1 | 8 | quartz | secondaries |
| | | 150-155(3) | -6.8 | 10.2 | quartz | secondaries |
| | | 145-150(3) | -9 | 12.8 | quartz | secondaries |
| | | 140-145(5) | | | quartz | secondaries |
| 195-205(5) | -2.2 | 3.7 | calcite that replaced anhydrite | secondaries | | |
| LR8-11 | 1390 | 155-160 | <-18 | >21 | calcite that replaced anhydrite | secondaries, Th max, clathrate present |
| | | 125-135(5) | <-18 | >21 | quartz | primaries near rim |
| | | 125-135(7) | <-18 | >21 | quartz | primaries near rim |
| | | 130-140(4) | <-18 | >21 | quartz | primaries near rim |
| | | 120-130(5) | <-18 | >21 | quartz | primaries near rim |
| LR8-11 | 1392 | 160-165 | <-18 | >21 | quartz | primary (possibly), Th max |
| | | 150-160 | >-7 | <10.5 | calcite that replaced anhydrite | secondaries, Th max |
| LR8-11 | 1393 | 150-160 | <-18 | >20 | quartz | primaries (possibly) |
| LR8-11 | 1743 | 180-185 | >-7 | <10.5 | calcite that replaced anhydrite | secondaries, Th max |
| LR8-11 | 1818 | 175-180(4) | | | calcite that replaced anhydrite | primaries |
| LR8-11 | 1942 | 185-195(3) | | | calcite that replaced anhydrite | primaries near outer growth zone with gas-filled inclusions |
| LR8-11 | 1984 | 175-185(4) | | | calcite that replaced anhydrite | secondaries, abundant gas-filled inclusions present |
| LR8-11 | 1989 | 205-210 | >-6 | <9.2 | calcite that replaced anhydrite | secondaries, Th max |

T_h = liquid-vapor homogenization temperature; T_m = final ice melting temperature; Salinities